Monthly Notices of the ROYAL ASTRONOMICAL SOCIETY

MNRAS **540,** 1608–1625 (2025) https://doi.org/10.1093/mnras/staf727
Advance Access publication 2025 May 31

Metallicity of active galactic nuclei from ultraviolet and optical emission lines – I. Carbon abundance dependence

O. L. Dors [1]★ C. B. Oliveira [1] M. V. Cardaci [2,3] G. F. Hägele,[2,3] I. N. Morais,[1] X. Ji [4,5] R. A. Riffel [6] R. Riffel [7] M. Mezcua [8,9] G. C. Almeida [1] P. C. Santos [1] and M. S. Z. de Mellos [6]

[1]*Universidade do Vale do Paraíba, Av. Shishima Hifumi, 2911, São José dos Campos, SP 12244-000, Brazil*
[2]*Facultad de Ciencias Astronómicas y Geofísicas, Universidad Nacional de La Plata, Paseo del Bosque s/n, La Plata 1900, Argentina*
[3]*Instituto de Astrofisica de La Plata (CONICET-UNLP), Avenida Centenario (Paseo del Bosque) S/N, La Plata B1900FWA, Argentina*
[4]*Kavli Institute for Cosmology, University of Cambridge, Madingley Road, Cambridge CB3 0HA, UK*
[5]*Cavendish Laboratory, University of Cambridge, 19 JJ Thomson Avenue, Cambridge CB3 0HE, UK*
[6]*Departamento de Física, Centro de Ciências Naturais e Exatas, Universidade Federal de Santa Maria, Santa Maria, RS 97105-900, Brazil*
[7]*Departamento de Astronomia, Universidade Federal do Rio Grande do Sul, Av. Bento Gonçalves 9500, Porto Alegre, RS, Brazil*
[8]*Institute of Space Sciences (ICE, CSIC), Campus UAB, Carrer de Magrans, E-08193 Barcelona, Spain*
[9]*Institut d'Estudis Espacials de Catalunya (IEEC), Carrer Gran Capita, E-08034 Barcelona, Spain*

Accepted 2025 April 30. Received 2025 April 29; in original form 2025 February 11

ABSTRACT

Metallicity (Z) estimates based on ultraviolet (UV) emission lines from the narrow-line regions of active galactic nuclei (AGNs) have been found to differ from those derived from optical lines. However, the origin of this discrepancy (ZR) remains poorly understood. To investigate the source of ZR, we compiled from the literature the fluxes of narrow near-UV [$1000 < \lambda(\text{Å}) < 2000$] and optical [$3000 < \lambda(\text{Å}) < 7000$] emission-line measurements for a sample of 11 AGNs (nine at $z < 0.4$ and two at $z \sim 2.4$). Metallicity values for our sample were derived using a semi-empirical calibration based on the $C43 = \log[(\text{C IV}\lambda1549 + \text{C III}]\lambda1909)/\text{He II}\lambda1640]$ emission-line ratio and compared with those obtained via direct measurement of the electron temperature (T_e-method) and via calibrations based on optical emission lines. The source of the discrepancy was investigated in terms of the ionization parameter (U), electron density (N_e), and carbon abundance (C/H). We found a weak correlation between ZR, U, and N_e. However, a moderate correlation was observed between ZR and direct estimates of C/H, suggesting that the previously assumed (C/O)–Z relations in photoionization models used to derive UV carbon-line calibrations may not be valid for AGNs. By combining a large set of abundance estimates for local star-forming regions with those of our AGN sample, we derived a new (C/O)–Z relation. Comparisons between the results of photoionization models that assume this new abundance relation and the UV observational data of our sample produce Z values derived from the $C43$ index that are consistent with those obtained using the T_e-method.

Key words: ISM: abundances – galaxies: abundances – galaxies: active – galaxies: nuclei.

1 INTRODUCTION

Recent observations of high-redshift systems by the *JWST* are providing important information on the metallicity (Z) of the gas phase of the earliest galaxies in the Universe. The specific Z pattern of a galaxy depends on the star formation history and chemical enrichment of its interstellar medium (ISM). Thus, Z estimates of objects at very high z uncover how the first stars formed and evolved and their interplay with the ISM in the early epoch of the Universe.

Due to the distance, most of the observed spectra of objects at $z > 6$ are in the ultraviolet (UV) wavelength range [$1000 < \lambda(\text{Å}) < 2000$], where emission-line ratios such as C III]λ1909/O III]λ1666 (e.g. Garnett et al. 1995a), N Vλ1240/He IIλ1640 (e.g. Hamann & Ferland 1992), and $C43 = (\text{C III}]\lambda1909 + \text{C IV}\lambda1549)/\text{He II}1640$ (Dors et al. 2014, 2019; Pérez-Montero et al. 2023) can be used as a Z tracer (see also Zhu, Kewley & Sutherland 2024). However, Z estimates through rest-frame UV lines are subject to several caveats:

(i) The unique hydrogen reference line in the UV spectrum is Lyα, a resonance line that can be enhanced by the presence of the He IIλ1215.1 and O V]λ1213.8, λ1218.3 emission lines (e.g. Shields, Ferland & Peterson 1995; Humphrey 2019). This fact results in imprecise dust reddening correction (generally not considered or taken from Balmer decrement) and forces us to use the He IIλ1640 emission line as a reference.

(ii) Photoionization models are generally employed to obtain calibrations between UV line ratios and Z. These calibrations are known as strong-line methods. In photoionization models it is required to assume pre-established abundance relations [e.g. (C/O)–(O/H), (N/O)–(O/H)] as input parameters. These abundance relations are barely known for high-z objects (e.g. Cameron et al. 2023; Isobe

★ E-mail: olidors@univap.br

et al. 2023; D'Eugenio et al. 2024; Ji et al. 2024; Rizzuti et al. 2024), resulting in not so well-established UV emission-line calibrations in comparison to the optical ones (e.g. Zhu et al. 2024).

(iii) Carbon and oxygen are depleted on to dust-grains in the diffuse ISM (e.g. Jenkins 2009) by uncertain factors and estimated mostly just for nearby star-forming regions (SFs: H II regions and H II galaxies; e.g. Garnett et al. 1995a, b; Peimbert & Peimbert 2010). This uncertainty can deeply impact on the derived Z values based on lines emitted by these elements by a factor of up to ~ 3 (e.g. see Roman-Duval et al. 2022 and references therein).

(iv) Any proposed method to estimate Z must be compared with direct estimates, i.e. with those via T_e-method,[1] the most reliable method (see e.g. Hägele et al. 2006, 2008; Toribio San Cipriano et al. 2017). Comparison between Z estimations based on UV lines and those through T_e-method has been carried out mainly for SFs (e.g. Byler et al. 2020).

Byler et al. (2020) found, for SFs located in a wide range of redshift ($0.04 > z \gtrsim 1.5$), that UV-based metallicities poorly correlate with those from optical lines. Additionally, Rigby et al. (2021) found, for the lensed galaxy SDSS J1723+3411 ($z = 1.3293$), that UV-only emission lines either cannot be used to estimate the metallicity or dramatically underestimate it. Finally, for the active galactic nucleus (AGN) system GS-3073 ($z \sim 5.5$) Ji et al. (2024), by using the T_e-method, derived log(N/O) abundance ratio values of ~ -1.1 and ~ 0.46 dex when optical and UV emission lines are considered, respectively. In general, Z values for SFs derived through UV lines are overestimated by up to $\sim$0.6 dex concerning those from optical lines (e.g. Byler et al. 2020; Mingozzi et al. 2022; Llerena et al. 2023). The source of such Z discrepancies has been mainly investigated for SFs and has been attributed to, for instance, the limitation in theoretical ionizing spectrum assumed in photoionization models and the contribution from stellar wind emission to the ISM enrichment (Byler et al. 2020).

Opposite to SFs, for AGNs a comparison between UV-based metallicities from strong-line methods and those from the T_e-method[2] is barely found in the literature. This is partially due to the lack of spectroscopic data, for the same sample of objects, taken in both UV and optical wavelength ranges (see table 2 of Dors et al. 2019). As noted in previous studies, the UV- and optical-based metallicities of AGNs, such as for SFs, seem to not conciliate with each other. For instance, no clear correlation between the metallicity of local universe AGNs ($z < 0.4$) and the host galaxy stellar mass ($M_\star$) is obtained when optical lines are employed in the Z derivation (e.g. Dors et al. 2020a; Peluso et al. 2023; Li et al. 2024). In opposite, UV-based metallicities of AGNs at high-z indicate a clear positive correlation with the $M_\star$ (e.g. Matsuoka et al. 2018; Dors et al. 2019). Although this disagreement can be due to the effects of completeness, redshift bias, and/or aperture effects of the AGN sample (e.g. Thomas et al. 2018a; Armah et al. 2023, 2024; Carr et al. 2023), part of it can be attributed to the methods employed in the Z estimation. For instance, calibrations between UV emission lines and Z have been obtained by using photoionization models (e.g. Nagao, Maiolino & Marconi 2006; Dors et al. 2014, 2019; Pérez-Montero et al. 2023; Zhu et al. 2024). In general, these models suffer limitations in the sense that the assumed abundance relations [e.g. (N/O)–(O/H), (C/O)–(O/H)], derived for local SFs and used as input parameters in photoionization models (e.g. Feltre, Charlot & Gutkin 2016), could deviate from those for AGNs (e.g. Baldwin et al. 2003; Dors et al. 2019; Ji & Yan 2020).

Pérez-Montero et al. (2023), by using the HII-CHI-MISTRY-UV code, which is based on a comparison between photoionization model results and observational spectroscopic data, found C/O abundances in local AGNs higher (by ~ 0.3 dex) than those for SFs with similar Z. Moreover, Nakajima & Maiolino (2022) pointed out that although the C/O and N/O abundance ratios are well established for H II regions, they are subject to significant dispersion, possibly caused by several processes including variations in star formation efficiency (e.g. Mollá et al. 2006) or gas exchange between galaxies and the surrounding intergalactic medium (e.g. Edmunds 1990; Köppen & Hensler 2005). This dispersion could also be increased by some systematic uncertainties at high redshift (see also Gutkin, Charlot & Bruzual 2016) and it is unknown for AGNs.

Additional discrepancy is also noted when UV and optical emission lines are used in the ionization parameter[3] (U) derivation. In fact, while U estimates through narrow optical emission lines of AGNs indicate log$U$ ranging from ~ -4.0 to ~ -2.5 dex (e.g. Castro et al. 2017; Carvalho et al. 2020; Carr et al. 2023), UV lines derivations result in higher ($-2.0 \lessapprox \log U \lessapprox -0.5$) U values (e.g. Nagao et al. 2006; Feltre et al. 2016; Dors et al. 2019; Pérez-Montero et al. 2023; Mingozzi et al. 2024). As in the case of the metallicity, the source of discrepancy in the ionization parameter derived from UV and optical lines remains unclear. U estimates significantly impact the derivation of Z, as emission-line ratios sensitive to Z can also depend on this nebular parameter (e.g. McGaugh 1991).

To investigate the AGN metallicity discrepancy derived when UV and optical emission lines are employed in the derivation of this parameter, in this study, we collected optical and UV emission-line fluxes of 11 objects from the literature and we derived their Z. We assumed as reference Z values derived through the T_e-method and from the empirical calibration relied on it proposed by Dors (2021). The Z discrepancy is investigated regarding its dependence on the electron density, ionization parameter, and carbon abundance. The paper is organized as follows. In Section 2 the methodology (observational data, metallicity, and elemental abundance estimates) are described. The results and discussion are presented in Section 3, while the conclusions in Section 4.

2 METHODOLOGY

To compare the AGNs gas-phase metallicities derived from UV and optical emission lines, the following methodology is assumed:

(i) For each object, fluxes of observational emission lines in the UV [$1000 < \lambda(\text{Å}) < 2000$] and optical [$3000 < \lambda(\text{Å}) < 7000$] wavelength ranges were compiled from the literature.

(ii) Observational line intensity ratios were used to estimate metallicities based on the T_e-method and strong-line methods.

(iii) Direct abundance estimates, nebular parameters, and photoionization models were employed to investigate the source of the metallicity discrepancy (if it exists) between estimates derived from UV and optical emission-line ratios.

The following subsections describe each step of the procedures outlined above.

[1]For a review of the T_e-method see Pérez-Montero (2017) and Peimbert, Peimbert & Delgado-Inglada (2017).

[2]For a comparison between oxygen abundance estimates of AGNs based on distinct optical emission lines see Dors et al. (2020a).

[3]The ionization parameter, U, is defined as the ratio of the flux of hydrogen-ionizing photons to the total hydrogen density.

Table 1. Object names, references from where the optical and UV emission lines were compiled, redshifts, and AGN classes. The logarithm of the X-ray luminosity (measured in the 14–195 keV band) values (when available) were taken from https://swift.gsfc.nasa.gov/results/bs70mon/.

Object	Reference		Redshift	Class	$\log(L_x)$ (erg s^{-1})
	Optical	Ultraviolet			
NGC 5506	Dopita et al. (2015)	Bergeron, Maccacaro & Perola (1981)	0.006084(1)	Seyfert 1.9(2)	43.31
NGC 1068	Koski (1978)	Snijders, Netzer & Boksenberg (1986)	0.003793(1)	Seyfert 2(2)	42.05
NGC 7674	Kraemer et al. (1994)	Kraemer et al. (1994)	0.029030(1)	Seyfert 2(3)	–
NGC 4507	Phillips, Charles & Baldwin (1983)	Bergeron et al. (1981)	0.011801(1)	Seyfert 2(2)	43.77
Mrk 3	Koski (1978)	Malkan & Oke (1983)	0.013509(1)	Seyfert 2(2)	43.76
Mrk 573	Koski (1978)	MacAlpine (1988)	0.017212(1)	Seyfert 2(3)	–
Mrk 1388	Osterbrock (1985)	MacAlpine (1988)	0.020954(1)	Seyfert 1.9(4)	–
MCG-3-34-64	Koss et al. (2021)	De Robertis, Hutchings & Pitts (1988)	0.016541(1)	Seyfert 1(4)	43.27
III Zw77	Ferland & Osterbrock (1987)	Ferland & Osterbrock (1987)	0.033829(1)	Seyfert 1.5(4)	–
4C+40.36	Humphrey et al. (2008)	Humphrey et al. (2008)	2.349(5)	radio galaxy(5)	–
4C+23.56	Humphrey et al. (2008)	Humphrey et al. (2008)	2.479(5)	radio galaxy(5)	–

Note. References: (1) https://ned.ipac.caltech.edu/. (2) Koss et al. (2021), (3) Osterbrock & Martel (1993), (4) Véron-Cetty & Véron (2006), (5) Humphrey et al. (2008).

2.1 Observational data

We compiled UV and optical emission lines from the literature for objects classified as AGNs. Their classifications were carried out by the authors of the original works from which the data were collected either by considering the presence of coronal emission lines emitted by elements with high ionization degree (e.g. [Ne V]λ3426, [Fe X]λ6374) or by using emission-line diagnostic diagrams (e.g. [O III]λ5007/H β versus [N II]λ6584/H α; Baldwin, Phillips & Terlevich 1981). We adopt the following criteria in the selection of AGNs.

(i) We only selected AGNs whose optical [O II]λ3726 + λ3729 (hereafter [O II]λ3727), H β, [O III]λ5007, H α, [N II]λ6584, [S II]λ6716, λ6731 and rest-frame UV C III]λ1909, C IV]λ1549, He IIλ1640 emission lines were measured. These emission lines allow us to estimate metallicities through strong-line methods (e.g. Storchi-Bergmann et al. 1998; Nagao et al. 2006; Dors et al. 2020a).

(ii) Although not used as a selection criterion, the fluxes of the optical [O III]λ4363 and [N II]λ5755 auroral lines, along with those of the Ly αλ1216, O III]λ1664, and C II]λ2325 lines, were compiled when available.

(iii) Additionally, when available, the fluxes of the He IIλ4686 and He Iλ5876 emission lines were compiled from the literature. These lines are necessary to estimate the ionization correction factor (ICF) of the oxygen (e.g. Flury & Moran 2020).

(iv) We consider only the narrow component of the lines above, i.e. H α or Ly α with full width at half-maximum lower than 1000 km s^{-1}. This criterion does select objects for which only low-velocity shocks (i.e. cloud–cloud collisions) can be present, hence gas dominated by highly turbulent material is not expected (e.g. Daltabuit & Cox 1972; Daltabuit, MacAlpine & Cox 1978; Dopita & Sutherland 1996; Bottorff et al. 2000; Foschini 2002; Mazzolari et al. 2024).

We found 11 AGNs that fulfil all the criteria above, being nine objects in the local universe ($z < 0.04$) and two objects at high redshift ($z \sim 2.4$). In Table 1 the selected AGNs together with the references from which the optical and UV spectroscopic data were compiled, their redshifts, AGN classification, and X-ray luminosities (when available) are listed.

Even though the selected objects were already classified as AGNs, we perform an additional classification that relied on the He IIλ4686/H β versus [N II]λ6584/H α diagram proposed by Shirazi & Brinchmann (2012). According to Molina et al. (2021), objects with

$$\log(\text{He II}\lambda4686/\text{H}\,\beta) \gtrsim -1.0 \quad (1)$$

are classified as AGNs and, otherwise, as SFs (see also Scholtz et al. 2023). In principle, this diagnostic diagram is more reliable than the classical [O III]λ5007/H β versus [N II]λ6584/H α (Baldwin et al. 1981) because the latter tends to misclassify as SFs those AGNs with $Z \lesssim 0.5\,Z_\odot$ (e.g. Groves, Heckman & Kauffmann 2006; Feltre et al. 2016; Hirschmann et al. 2023; Dors et al. 2024a; Mazzolari et al. 2024) that, in general, are located in galaxies with low mass ($M_\star \lesssim 10^{9.5}\,M_\odot$, e.g. Izotov & Thuan 2008; Bykov, Gilfanov & Sunyaev 2024; Mezcua & Domínguez Sánchez 2024). In Fig. 1, bottom left panel, the He II/H β versus [N II]/H α diagram containing the observational data of our sample is shown. In this diagram all objects occupy the AGN regions, while in the [O III]/Hβ versus [N II]/H α diagnostic diagram (top left panel of Fig. 1) one object of our sample, III Zw77, is located in the zone occupied by SFs, below the maximum starburst lines proposed by Kauffmann et al. (2003) and Kewley et al. (2006). III Zw77 presents a very low $N2 = \log([\text{N II}]\lambda6584/\text{H}\,\alpha)$ line intensity ratio that, according to the Z–$N2$ calibration proposed by Carvalho et al. (2020), corresponds to $Z \lesssim 0.2\,Z_\odot$. In Fig. 1, right panel, a log(C III]λ1909/He IIλ1640) versus log(C IV]λ1549/C III]λ1909) diagram containing our observational data (blue points) is shown. The horizontal black line defines the empirical separation between AGNs and SFs where, according to Dors et al. (2018), objects with

$$\log(\text{C III}]\lambda1909/\text{He II}\lambda1640) \lesssim 0.5 \quad (2)$$

are classified as AGNs, otherwise, SFs (see also Hirschmann et al. 2019). It is evident that all objects in our sample lie within the AGN zone, thereby corroborating their prior classifications.

The literature-compiled optical line intensity ratios were already corrected by Galactic and internal extinction. Different approaches to the dust effects could result in distinct reddening correction functions yielding different line intensity ratios. However, Dors et al. (2022) showed that the uncertainty in emission-line ratios resulting from different approaches to the extinction correction is comparable to that caused by errors in emission-line measurements (~ 0.1 dex, e.g. Kennicutt, Bresolin & Garnett 2003). Regarding the UV lines, following Nagao et al. (2006), no internal reddening correction (or only Galactic extinction correction) was applied to the fluxes of the involved emission lines. This procedure was adopted because the emission lines have close wavelengths, the objects are mostly

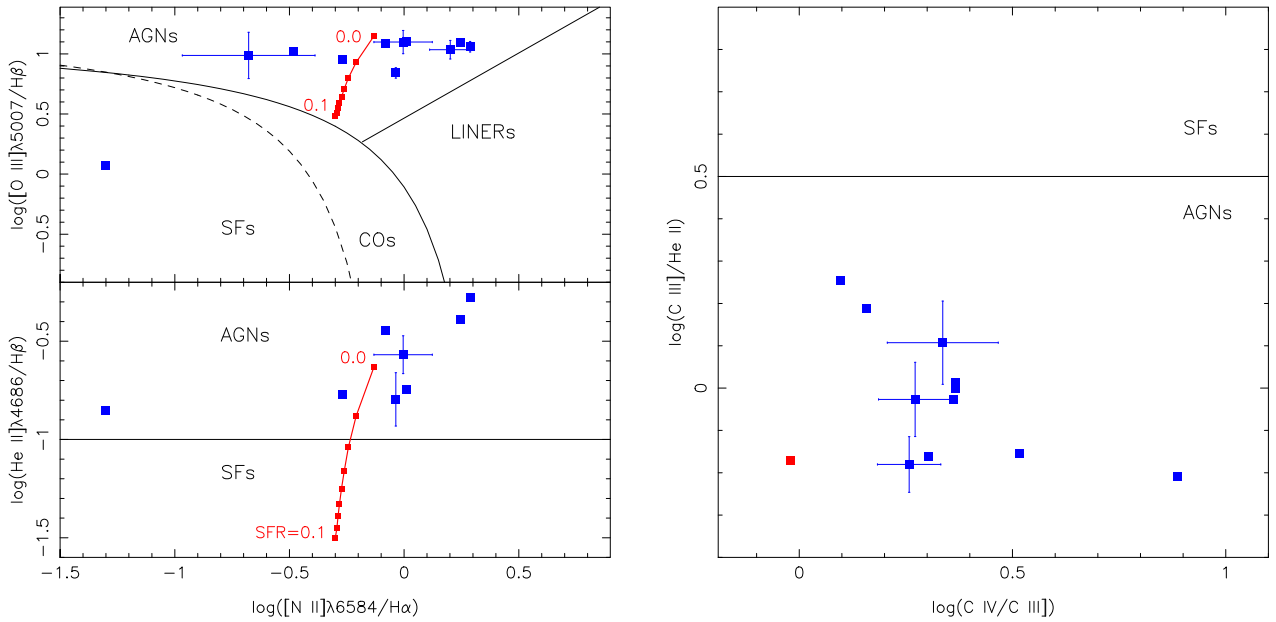

Figure 1. Diagnostic diagrams used to identify AGN-like and SF-like objects. The blue points represent observational data of our sample of AGNs (see Section 2.1). Bottom left panel: He IIλ4686/H β versus [N II]λ6584/H α diagram suggested by Shirazi & Brinchmann (2012). The line represents the separation criterion suggested by Molina et al. (2021) and given by equation (1). Upper left panel: [O III]λ5007/H β versus [N II]λ6584/H α (Baldwin et al. 1981). The dashed and solid curves represent the empirical and theoretical separation criteria suggested by Kauffmann et al. (2003) and Kewley et al. (2006), respectively. The region between the Kauffmann et al. (2003) and Kewley et al. (2006) curves is occupied by composite objects (COs). The solid line represents the criterion suggested by Kewley et al. (2006) to separate AGNs from LINERs. In the left panels, the red line connects the results of photoionization models simulating composite (AGN + SF) objects (see Section 2.1). The SFR (in units of $M_\odot$ yr^{-1}) of the simulated COs is indicated. Right panel: C III]λ1909/He IIλ1640 versus C IV]λ1549/C III]λ1909 suggested by Hirschmann et al. (2019). The line corresponds to the empirical separation criterion suggested by Dors et al. (2018) and given by equation (2). Composite model results are represented by only one red point, since the AGN luminosity of the UV lines considered is higher (by $\sim$ 0.3 dex) in comparison to those of CNSFRs (see Table 2).

face-on, and only one hydrogen line (Ly α) is measured in the UV spectrum. It is worth mentioning that, for our sample, it is not possible to carry out reddening correction by using the He IIλ1640/λ4686 line ratio (e.g. Bergeron et al. 1981), hence for most of the objects the absolute UV emission-line fluxes are not available. In any case, we noted in the studies in which the data were compiled such that the effect of extinction correction in the line ratios considered here is lower than the uncertainty ($\sim$ 30 per cent) on them (see Ferland & Osterbrock 1987). In fact, for instance, considering the UV data for NGC 7674 (one object of our sample) from Kraemer et al. (1994), the observational C III]λ1909/Ly α line ratio is 0.17 ± 0.09, while the reddening-corrected value is 0.12 ± 0.06.

One concern in this study is that the optical and UV spectra for the same object were obtained using different instruments, which may lead to distinct extraction apertures (e.g. Humphrey et al. 2008). Differences in observational set-ups may be sources of discrepancies in the derived parameters through optical and UV line fluxes (e.g. Berg et al. 2024). In particular, emission from nuclear H II regions can contribute by distinct amounts to the observed UV and optical AGN spectra. For instance, Thomas et al. (2018b) fitted photoionization model results to observational emission-line intensity ratios of 2766 Seyfert galaxies, whose data were taken from the Sloan Digital Sky Survey Data Release 7 (Abazajian et al. 2009). These authors found that, even for AGNs with high ionization degree, i.e. log([O III]λ5007/Hβ) $\gtrsim$ 0.9, about 30 per cent of the Balmer flux arises from H II regions (see also de Mellos et al. 2024). However, Humphrey et al. (2008), who analysed the aperture effect on emission-line measurements for a sample of high-z galaxies, found that the size of the aperture does not influence line intensity ratios by more than 10 per cent (see also Daltabuit & Cox 1972; Kewley, Jansen & Geller 2005; Mannucci et al. 2021; Arellano-Córdova et al. 2022; Pilyugin et al. 2022). It is worth mentioning that the objects analysed by Humphrey et al. (2008) are at $z \sim 2.4$, where the impact of aperture on emission-line fluxes is lower compared to that on local AGNs (e.g. Davies et al. 2016; D'Agostino et al. 2019a; Pilyugin et al. 2020; Hviding et al. 2023; Molina et al. 2023).

To investigate the flux contribution from H II regions to the observed spectrum of an AGN, we built photoionization models using version 23.01 of the CLOUDY code (Ferland et al. 2017) and following a similar methodology to the one adopted by Dors et al. (2018). In particular, we considered an AGN surrounded by eight circumnuclear star-forming regions (CNSFRs) as illustrated in Fig. 2. The nebular parameters adopted in the models are summarized in what follows:

(i) CNSFR models: We assumed solar metallicity, electron density $N_e = 200$ cm^{-3} (see e.g. Copetti et al. 2000), spherical geometry, inner radius of 3 pc, and the logarithm of the number of ionizing photons log Q(H)[s^{-1}] = 51, being about the mean value derived by Díaz et al. (2007) for CNSFRs in the NGC 2903, NGC 3351, and NGC 3504 galaxies. We considered as the ionizing source a stellar cluster instantaneously formed, with an age of 3.5 Myr, stellar mass of 10^6 $M_\odot$, initial mass function as defined by Kroupa (2002), and a spectrum taken from the STARBURST99 code (Leitherer et al. 1999). These nebular and stellar parameters are typical of CNSFRs in nearby galaxies as derived by Díaz et al. (2007) and Dors O. L. et al. (2008).

(ii) AGN models: We assumed an electron density N_e = 500 cm^{-3}, $Z = Z_\odot$, log Q(H)[s^{-1}] = 51, spherical geometry, inner radius of 3 pc, and a power law with the optical to X-rays slope $\alpha_{ox} = -1.1$ (Tananbaum et al. 1979) as the ionizing source. These

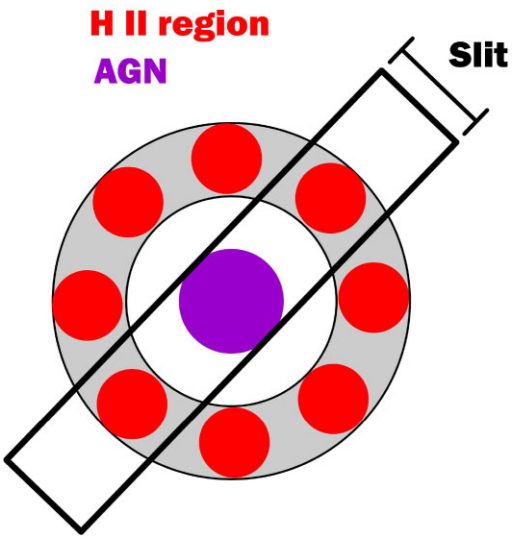

Figure 2. Illustration of a galaxy nuclei containing an AGN and CNSFRs, as indicated. This scenario is used to investigate the flux contribution of H II regions to the spectrum of an AGN obtained by distinct slit apertures, as indicated (see Section 2.1).

Table 2. Logarithm of the luminosity [$L(\lambda)$; in erg s^{-1}] of some emission lines predicted by the pure-AGN and CNSFR photoionization models. Both types of models assume as input parameters the logarithm of the number of ionizing photons log Q(H)[s^{-1}] = 51, electron density equal to 500 cm^{-3}, spherical geometry, and solar metallicity (see Section 2.1).

Line	log[L(λ)]	
	pure-AGN	CNSFR
H β	38.64	38.55
He IIλ4686	38.01	33.09
[O III]λ5007	39.79	38.69
H α	39.09	39.00
[N II]λ6584	38.96	38.67
C IVλ1549	38.72	36.54
He IIλ1640	38.91	34.90
C III]λ1909	38.74	36.69

parameters are typical of local AGNs as derived through photoionization models simulating narrow-line regions (NLRs; e.g. Dors O. L. et al. 2017; Pérez-Montero et al. 2019).

In Table 2, the resulting luminosity values for the optical and UV lines involved in the diagrams presented in Fig. 1, and predicted by the pure AGN and CNSFR models, are listed.

By using the predicted pure-AGN and CNSFR luminosity values listed in Table 2, we simulated distinct slit apertures encompassing one by one each CNSFR. The resulting line intensity ratio was considered as

$$\frac{I(\lambda_1)}{I(\lambda_2)} = \frac{L(\lambda_1)_{\rm AGN} + n \times L(\lambda_1)_{\rm H\,II}}{L(\lambda_2)_{\rm AGN} + n \times L(\lambda_2)_{\rm H\,II}}, \quad (3)$$

being $I(\lambda_1)/I(\lambda_2)$ the intensity ratio of two emission lines, L the luminosity of a given emission line predicted by the photoionization models, and n the number of H II regions. The value $n = 0$ represents the emission-line ratio of a pure AGN and $n = 8$ the number of CNSFRs as observed, for instance, in NGC 3351 (Díaz et al. 2007; Hägele et al. 2007, 2010). In Fig. 1, left panels, the results of our simulations in the [O III]/Hβ versus [N II]/Hα and He II/Hβ versus [N II]/Hα diagnostic diagrams are shown. In these figures, the photoionization model results are shown in terms of star formation rate (SFR), calculated through the predicted CNSFR model values of L(H α) and from the largely used relation by Kennicutt (1998):

$$\mathrm{SFR(M_\odot\ yr^{-1})} = 7.9 \times 10^{-42}\ L^{\rm T}(\mathrm{H}\,\alpha)\ [\mathrm{erg\ s^{-1}}], \quad (4)$$

being $L^{\rm T}(\mathrm{H}\alpha) = n \times L(\mathrm{H}\alpha)_{\rm H\,II}$. It can be seen in left panels of Fig. 1 that the simulation results indicate that the flux contribution from CNSFRs to the spectra of our object sample could be negligible, hence models without star formation would describe almost all our observational data. This result is expected, as the majority of the objects in our sample are AGNs characterized by a high degree of ionization [log([O III]λ5007/Hβ) $\sim$ 1].

The above result is also supported by the simulation of composite (AGN + SF) objects by Thomas et al. (2018b), since our objects are located in the zone of their [O III]/Hβ versus [N II]/H α diagram corresponding to SF contributions to the emission-line ratio intensities of less than $\sim$ 20 per cent (see also Agostino et al. 2021; Vidal-García et al. 2024). In Fig. 1, right panel, results from our simulation (red point) are shown in the UV diagnostic diagram. We found that the values of the C III]/He II and C IV/C III] emission-line ratios practically do not change due to flux contributions from CNSFRs. This result is expected, since the AGN luminosity of the UV lines considered is higher by a factor ranging from $\sim$ 0.2 to $\sim$ 0.4 dex in comparison to those from CNSFRs (see Table 2). Thus, it is able to argue that we are analysing spectroscopic data of 'almost' pure-AGNs.

In Table 3, optical (in relation to H $\beta = 1.0$) and the UV (in relation to He IIλ1640 = 1.0) line intensity ratios for our AGN sample are listed. As it was mentioned before, only for the optical lines the reddening correction was carried out.

2.2 Photoinization models

For the purpose of our analysis, we built an extensive grid of photoionization models using version 23.01 of the CLOUDY code (Ferland et al. 2017) to simulate NLR of AGNs. We apply the same methodology as in Dors et al. (2022). The adopted nebular parameters are described below.

(i) Spectral energy distribution (SED): We consider SEDs parametrized by the continuum between 2 keV and 2500Å (Tananbaum et al. 1979) and described by a power law with a spectral index α_{ox} ranging from −1.5 to −0.8, with a step of 0.1. Results of photoionization models assuming this α_{ox} range reproduce optical (e.g. Carvalho et al. 2020; Ji et al. 2020) and UV (e.g. Dors et al. 2014, 2019) narrow emission lines of AGNs.

(ii) Metallicity (Z): We consider the metallicity in relation to the solar one ($Z/Z_\odot$) in the range of 0.2–3.0, with a step of 0.2. This metallicity range is similar to the one derived through the T_e-method for local Seyfert nuclei (e.g. Dors et al. 2020b).

(iii) Abundance relations: We adopt the (N/O)–(O/H) abundance relation given by log(N/O) = [1.29 × (12 + log(O/H))] − 11.84 derived by Carvalho et al. (2020) and representative for local AGNs. For the C-O relation, we assumed

$$(\mathrm{C/H}) = 6.0 \times 10^{-5} \times (Z/Z_\odot) + 2.0 \times 10^{-4} \times (Z/Z_\odot)^2 \quad (5)$$

derived for H II regions by Dopita et al. (2006). For the helium, we assumed the 12 + log(He/H) = 0.1215 × [12 + log(O/H)]^2 − 1.8183 × [12 + log(O/H)] + 17.6732 derived by Dors et al. (2022) by using the T_e-method. Other elements were linearly scaled with the metallicity. Following Nagao et al. (2006), who found that photoionization models with dust grains predict line flux ratios, which are in disagreement with most of the observed values, our

Table 3. Intensities of optical (relative to H $\beta = 1.0$) and UV (relative to He IIλ1640 $= 1.0$) emission lines taken from the literature (see Table 1). Only the optical line ratios are reddening-corrected. The [C II]λ2325 emission line corresponds to the sum of λ2323.50, λ2324.69, λ2325.40, λ2326.93, and λ2328.12Å lines.

Line	NGC 5506	NGC 1068	NGC 7674	NGC 4507	Mrk 3	Mrk 573	Mrk 1388	MCG-3-34-64	III Zw77	4C + 40.36	4C + 23.56
					Optical (relative to H$\beta = 1.0$)						
[O II]λ3727	2.64 ± 0.03	1.23	1.29 ± 0.27	2.75	3.52	2.92	0.79	2.73 ± 0.03	0.15	4.26 ± 0.66	2.57 ± 1.24
[O III]λ4363	0.11 ± 0.004	0.22	0.12 ± 0.03	0.35	0.24	0.18	0.69	0.27 ± 0.003	0.16	–	–
H β	1.00 ± 0.01	1.00	1.00	1.00	1.00	1.00	1.00	1.00	1.00	1.00	1.00
He IIλ4686	0.16 ± 0.05	0.41	0.27 ± 0.06	0.17	0.18	0.36	–	0.53 ± 0.006	0.14	–	–
[O III]λ5007	6.95 ± 0.04	12.42	12.55 ± 2.51	8.91	12.67	12.12	10.53	11.48 ± 0.12	1.17	10.85 ± 1.60	9.71 ± 4.20
[N II]λ5755	0.02 ± 0.05	0.02	–	–	0.05	–	–	–	–	–	–
He Iλ5876	0.11 ± 0.18	0.15	–	–	0.08	0.10	0.09	0.18 ± 0.005	0.07	–	–
H α	2.86 ± 0.02	2.57	3.70 ± 0.78	2.83	3.10	2.95	2.84	2.86 ± 0.03	2.84	2.94 ± 0.43	2.85 ± 1.24
[N II]λ6583	2.65 ± 0.02	4.55	3.68 ± 0.77	1.53	3.18	2.47	0.95	5.55 ± 0.05	0.14	4.70 ± 0.69	0.60 ± 0.32
[S II]λ6716	0.94 ± 0.01	0.26	0.54 ± 0.11	0.58	0.73	0.75	0.21	0.78 ± 0.01	0.02	–	–
[S II]λ6731	1.06 ± 0.01	0.55	0.64 ± 0.13	0.64	0.82	0.80	0.18	0.93 ± 0.01	0.02	–	–
					Ultraviolet (relative to He IIλ1640 $= 1.0$)						
Ly α	–	3.81 ± 0.79	9.15	13.65	7.11	12.00	12.94	5.56	11.11	14.87 ± 1.25	5.06 ± 0.34
He IIλ1640	1.00	1.00	1.00	1.00	1.00	1.00	1.00	1.00	1.00	1.00	1.00
O III]λ1664	–	0.11 ± 0.04	–	–	–	–	–	–	0.87	0.16 ± 0.02	0.26 ± 0.03
C IVλ1549	2.25	2.78 ± 0.60	2.23	2.41	2.33	2.30	2.17	1.39	4.77	1.76 ± 0.15	1.20 ± 0.15
C III]λ1909	1.80	1.28 ± 0.27	1.54	1.03	1.00	0.70	0.94	0.69	0.62	0.94 ± 0.17	0.66 ± 0.08
[C II]λ2325	–	0.28 ± 0.06	–	0.46	1.00	–	–	–	–	0.56 ± 0.06	0.52 ± 0.06

models are dust-free. However, other studies (e.g. Groves, Dopita & Sutherland 2004; Feltre et al. 2016) include dust in their models to reproduce observations.

(iv) Electron density (N_e): We assume N_e values in the range of 100–5000 cm^{-3} (step of 100 cm^{-3}), typical of NLRs (e.g. Zhang 2024).

In total, the grid contains 69 600 photoionization models.

2.3 Strong-line method

2.3.1 UV calibration

We consider a semi-empirical calibration between fluxes of UV emission lines and the metallicity proposed by Dors et al. (2019). This calibration was obtained by comparing the results of photoionization models, simulating NLRs, with narrow UV emission-line intensity ratios of 77 AGNs with redshifts between 0 and 3.8, divided in Seyfert 2s (nine objects), high-z radio galaxies (61 objects), radio-quiet type-2 (one object), and type-2 quasars (six objects). The semi-empirical calibration is

$$\begin{aligned}(Z/Z_\odot) = {} & (2.13_{\pm 0.09}) + (2.41_{\pm 0.19})\, x^2 + (4.76_{\pm 0.58})\, C43^2 \\ & + (7.79_{\pm 0.59})\, x\, C43 - (4.64_{\pm 0.19})\, x \\ & - (5.64_{\pm 0.48})\, C43, \end{aligned} \quad (6)$$

where $C43 = \log[(\text{C IV}\lambda1549 + \text{C III}]\lambda1909)/\text{He II}\lambda1640]$ and $x = C3C4 = \log(\text{C III}]\lambda1909/\text{C IV}\lambda1549)$. This calibration is valid for the range of $-2 \lesssim C43 \lesssim 1$, which translates to $0.2 \lesssim (Z/Z_\odot) \lesssim 4$.

Also, Dors et al. (2019) proposed the following semi-empirical calibration to derive the ionization parameter:

$$\begin{aligned}\log U = {} & -(0.14_{\pm 0.02}) \times C3C4^2 - (1.10_{\pm 0.01}) \\ & \times C3C4 - (1.80_{\pm 0.01}), \end{aligned} \quad (7)$$

valid for the $-1 \lesssim C3C4 \lesssim 0.5$ range, which corresponds to $-2.5 \lesssim \log U \lesssim -1.0$.

The photoionization models assumed by Dors et al. (2019) consider a fixed value of $N_e = 500$ cm^{-3}, a nitrogen–metallicity relation

$$(\text{N}/\text{N}_\odot) = 4.5 \times (Z/Z_\odot)^{1.2}, \quad (8)$$

and a fixed value of

$$\log(\text{C}/\text{O}) = -0.50. \quad (9)$$

It is worth mentioning that Dors et al. (2019) tested various abundance relations and only the photoionization models that assumed the relations mentioned above successfully reproduced the UV emission-line ratios of their sample of 77 AGNs. Although these authors had also proposed a calibration between N Vλ1240/He IIλ1640 and Z, the intensity of this nitrogen line is available for a few objects of our sample and was not considered here.

2.3.2 Optical calibrations

We consider distinct calibrations between the intensities of optical emission-line ratios and metallicity. The first one is the empirical calibration proposed by Dors (2021):

$$Z = (-1.00_{\pm 0.09})\text{P} + (0.036_{\pm 0.003})R_{23} + (8.80_{\pm 0.06}), \quad (10)$$

where $Z \equiv 12 + \log(\text{O}/\text{H})$, $R_{23} = ([\text{O II}]\lambda3727 + [\text{O III}]\lambda4959 + \lambda5007)/\text{H}\,\beta$, and $P = ([\text{O III}]\lambda4959 + \lambda5007/\text{H}\,\beta)/R_{23}$. This calibration, valid for the range of $5 \lesssim R_{23} \lesssim 20$ or $0.3 \lesssim (Z/Z_\odot) \lesssim 2.0$, was obtained by using narrow emission-line intensity ratios of a large sample of 109 AGNs (Seyfert 1s and 2s) and direct estimates of O/H based on the T_e-method. This calibration yields O/H values somewhat lower (~ 0.2 dex) than those derived from photoionization models (a strong-line method) and, in principle, its use results in O/H values similar to those derived using the T_e-method.

It must be noted that P can be also written as a function of $O32 = [\text{O III}]\lambda5007/[\text{O II}]\lambda3727$), i.e. $P = O32/(1 + O32)$, which is related with the ionization parameter U, see discussion below. With this in mind, equation (10) implies that the metallicity derived via this calibration depends on the ionization parameter as well as the R_{23} index (e.g. McGaugh 1991).

The second relation is the semi-empirical calibration between $N2 = \log([\mathrm{N\,II}]\lambda6584/\mathrm{H}\alpha)$ and Z proposed by Carvalho et al. (2020). These authors compared the results of photoionization models simulating NLRs with spectroscopic data of confirmed Seyfert 2 nuclei finding

$$(Z/Z_{\odot}) = 4.01^{N2} - 0.07, \tag{11}$$

valid for the range of $-0.7 \lesssim N2 \lesssim 0.6$, which translates to $0.3 \lesssim (Z/Z_{\odot}) \lesssim 2.0$.

Carvalho et al. (2020) also proposed a semi-empirical calibration to estimate the ionization parameter given by

$$\log U = [0.57 \times (\log O32)^2] + [1.38 \times \log O32] - 3.14, \tag{12}$$

where $O32 = [\mathrm{O\,III}]\lambda5007/[\mathrm{O\,II}]\lambda3727$. This calibration is valid for the range of $-1.5 \lesssim O32 \lesssim 1.0$, which translates to $-4.0 \lesssim \log U \lesssim -2.0$.

2.3.3 Zhu et al. calibrations

Zhu et al. (2024), by using the MAPPINGS code (Sutherland et al. 2018), built a grid of photoionization models simulating NLRs of AGNs. Briefly, these models assume plane-parallel geometry, distinct values for the gas pressure, dust content, metallicity in the range of $7.2 \lesssim 12 + \log(\mathrm{O/H}) \lesssim 9.5$ [$0.03 \lesssim (Z/Z_{\odot}) \lesssim 6.5$], and $\log U$ ranging from -3.8 to -1.0. The (C/O)–(O/H) relation assumed in the models by Zhu et al. (2024) is that derived from stellar data by Nicholls et al. (2017) and represented by

$$\log(\mathrm{C/O}) = \log(10^{-0.8} + 10^{[\log \mathrm{O/H} + 2.72]}). \tag{13}$$

The discrepancy between the emission-line ratios calculated by the CLOUDY and MAPPINGS codes can differ by ~ 0.1 dex (D'Agostino et al. 2019b; Zhu et al. 2023).

Concerning the $C43$ calibration by Zhu et al. (2024), these authors showed that Z values estimated through their calibrations are consistent with those above by a factor lower than ~ 0.1 dex. From the several theoretical calibrations proposed by Zhu et al. (2024), we consider the ones between the $C3C4$ and $O32$ lines ratios and $\log U$, whose equations are presented in table 5 of Zhu et al. (2024).

The uncertainty in O/H abundance estimates obtained via strong-line methods, calculated from the errors of observational emission-line fluxes and the fitting coefficients of calibrations, is in order of ~ 0.2 dex, which translates into an uncertainty of ~ 50 per cent in Z estimates (e.g. Kobulnicky, Kennicutt & Pizagno 1999; Denicoló, Terlevich & Terlevich 2002; Dors et al. 2017; Zhu et al. 2024). The uncertainty in U estimates derived from the comparison between photoionization models and AGN observational data is ~ 0.15 dex (e.g. Dors et al. 2019; Pérez-Montero et al. 2019).

The uncertainty values above are considered in the Z and U estimates from the strong emission-line methods assumed in this study.

2.4 T_e-method

We estimated, for each object of our sample of AGNs, the total abundance of the oxygen and carbon (in relation to hydrogen) through the T_e-method and by using the 1.1.13 version of the PYNEB code (Luridiana, Morisset & Shaw 2015).

2.4.1 Oxygen abundance

The ionic abundances for the oxygen were calculated according to

$$\frac{\mathrm{O^+}}{\mathrm{H^+}} = f\left(\frac{[\mathrm{O\,II}]\lambda3727}{\mathrm{H}\beta}, T_{\mathrm{low}}, N_{\mathrm{e}}\right) \tag{14}$$

and

$$\frac{\mathrm{O^{2+}}}{\mathrm{H^+}} = f\left(\frac{[\mathrm{O\,III}]\lambda5007}{\mathrm{H}\beta}, T_{\mathrm{high}}, N_{\mathrm{e}}\right). \tag{15}$$

Values for N_e and T_{high} were obtained from the [S II]$\lambda6716/\lambda6731$ and [O III]$(\lambda4959 + \lambda5007)/\lambda4363$ line ratios, respectively, where the theoretical ratio [O III]$(\lambda4959/\lambda5007) = 0.33$ (Storey & Zeippen 2000) was considered. The value for T_{low} was obtained either from [N II]$(\lambda6548 + \lambda6584)/\lambda5755$ (3/11 objects) or from the theoretical relation proposed by Dors et al. (2020b):

$$t_{\mathrm{low}} = \left(\mathrm{a} \times t_{\mathrm{high}}^3\right) + \left(\mathrm{b} \times t_{\mathrm{high}}^2\right) + (\mathrm{c} \times t_{\mathrm{high}}) + \mathrm{d}, \tag{16}$$

where $\mathrm{a} = 0.17$, $\mathrm{b} = -1.07$, $\mathrm{c} = 2.07$, and $\mathrm{d} = -0.33$, while t_{low} and t_{high} represent T_{low} and T_{high}, respectively, in units of 10^4 K.

To calculate the total oxygen abundance (O/H) we adopted the following approach:

$$\frac{\mathrm{O}}{\mathrm{H}} = \mathrm{ICF}(\mathrm{O^+ + O^{2+}}) \times \left[\frac{\mathrm{O^+}}{\mathrm{H^+}} + \frac{\mathrm{O^{2+}}}{\mathrm{H^+}}\right]. \tag{17}$$

To derive the oxygen ICF, we assume the usual approach (see Izotov et al. 2006; Flury & Moran 2020; Dors et al. 2022):

$$\mathrm{ICF}(\mathrm{O^+ + O^{2+}}) = \frac{\mathrm{He^+ + He^{2+}}}{\mathrm{He^+}}, \tag{18}$$

being $\mathrm{He^+/H^+}$ and $\mathrm{He^{2+}/H^+}$ the ionic abundance ratios derived from the observational He I$\lambda5876/\mathrm{H}\beta$ and He II$\lambda4686/\mathrm{H}\beta$ line intensity ratios, respectively, measured in the spectrum of each object (see Table 3). For objects for which it is not possible to derive the $\mathrm{ICF}(\mathrm{O^+ + O^{2+}})$ due to the lack of helium line measurements (see Table 3), a mean ICF value equal to 1.5, as derived by Dors et al. (2022) for a large sample of local AGNs, was considered.

2.4.2 Carbon abundance

The carbon abundance estimates, based on UV emission lines, suffer large uncertainties due to the need of using the Lyα as a reference line, hence it is a resonance line undergoing a complex radiative transfer (e.g. Laursen, Razoumov & Sommer-Larsen 2009) and it could be blended with geocoronal hydrogen emission (e.g. Bergeron et al. 1981). Due to these caveats, we estimated the ionic abundances by adopting a distinct methodology from the one used by previous studies (e.g. Garnett et al. 1995a; Berg et al. 2019), in which the C/O abundance is calculated through the C III]$\lambda1909$/O III]$\lambda1664$. In this study, we estimated the $\mathrm{C^{2+}}$ and $\mathrm{C^{3+}}$ ionic abundances in relation to the $\mathrm{He^+}$ derived from the C III]$\lambda1909$/He II$\lambda1640$ and C IV$\lambda1549$/He II$\lambda1640$ line ratios, respectively, combined with the $\mathrm{He^{2+}/H^+}$ optical abundance estimates. In this regard, initially, we estimated the carbon ionic abundances as

$$\frac{\mathrm{C^{2+}}}{\mathrm{He^{2+}}} = \frac{F(\mathrm{C\,III}]\lambda1909)}{F(\mathrm{He\,III}\lambda1640)} \times \frac{\epsilon_{\lambda1640}(N_{\mathrm{e}}, T_{\mathrm{e}})}{\epsilon_{\lambda1909}(N_{\mathrm{e}}, T_{\mathrm{e}})} \tag{19}$$

and

$$\frac{\mathrm{C^{3+}}}{\mathrm{He^{2+}}} = \frac{F(\mathrm{C\,IV}\lambda1549)}{F(\mathrm{He\,II}\lambda1640)} \times \frac{\epsilon_{\lambda1640}(N_{\mathrm{e}}, T_{\mathrm{e}})}{\epsilon_{\lambda1549}(N_{\mathrm{e}}, T_{\mathrm{e}})}, \tag{20}$$

where F and ϵ are the measured flux and the emissivity, respectively, of the indicated emission lines. Using the PYNEB code, assuming an

electron density of $N_e = 500$ cm^{-3} (typical of NLRs, e.g. Dors et al. 2020a; Zhang 2024), and a range of electron temperature from 5000 to 25 000 K, we obtained

$$\frac{\epsilon_{\lambda 1640}}{\epsilon_{\lambda 1909}} = 0.05 \times (t_{\rm high}^{-7.00}) \quad (21)$$

and

$$\frac{\epsilon_{\lambda 1640}}{\epsilon_{\lambda 1549}} = 0.03 \times (t_{\rm vhigh}^{-8.79}), \quad (22)$$

where $t_{\rm high}$ and $t_{\rm vhigh}$ are the electron temperature of the high and very high ionization zones, respectively, in units of 10^4 K. Then, the total carbon abundance in relation to the hydrogen is obtained by

$$\frac{\rm C}{\rm H} = \left(\frac{\rm He^{2+}}{\rm H^{+}}\right)_{\rm op.} \times {\rm ICF(C^{2+} + C^{3+})} \times \left[\frac{\rm C^{2+}}{\rm He^{2+}} + \frac{\rm C^{3+}}{\rm He^{2+}}\right], \quad (23)$$

where the $({\rm He^{2+}/H^{+}})_{\rm op.}$ is the abundance ratio derived from optical lines and by using the T_e-method.

The temperature supposition for distinct carbon ions is not as direct as for the oxygen (e.g. Hägele et al. 2008). According to the four-zone ionization model proposed by Berg et al. (2021), the gas structure in H II regions can be divided into low, intermediate, high, and very high ionization zones. Under this scenario, C^{3+} (PI = 64.49 eV) occupies preferably the very high ionization zone, whose temperature is here defined by $T_{\rm vhigh}$. Direct estimates of this temperature can be obtained through a ratio between lines emitted by the Ne^{2+} ion (PI = 63.45 eV), i.e. [Ne III]λ3342/λ3868, which is unfortunately not available for our data sample. The C^{2+} ion (PI = 47.88 eV) partially spans on both intermediate and high ionization zones, thus, the temperature for this ion is similar to the one for O^{2+} (PI = 35.12 eV, see Garnett et al. 1995a).

As shown by Dors et al. (2020b), AGNs and H II regions tend to present distinct temperature structures, thus, not necessarily the four zones model proposed by Berg et al. (2021) is valid for our analysis. To test its validity, we use the electron temperature values for the C^{3+}, C^{2+}, and O^{2+} ions predicted by the AGN photoionization model results described above. We assume the mean temperature values calculated over the nebular AGN radius times the electron density. In Fig. 3, the model-predicted temperatures (in units of 10^4 K) for C^{3+} and C^{2+} versus those for O^{2+} are plotted in terms of $\log U$. The dashed line indicates the equality between the estimates and the error bars the typical electron temperature uncertainty of ±1000 K (e.g. Dors et al. 2023). It can be seen that the models, assuming this estimation for the temperature uncertainty, predict $T_e(C^{3+})$ values very similar to $T_e(O^{2+})$ ones, although a slight deviation in comparison to the one-by-one relation is noted. $T_e(C^{2+})$ is systematically lower than $T_e(O^{2+})$ for O^{2+} temperature values higher than ∼ 20 000 K. A fitting to the model temperature predictions in Fig. 3 provide

$$y = -0.212(\pm 0.003)x^2 + 1.342(\pm 0.008)x - 0.171(\pm 0.006) \quad (24)$$

and

$$w = -0.055(\pm 0.003)x^2 + 1.213(\pm 0.008)x - 0.101(\pm 0.006), \quad (25)$$

where $y = t_e(C^{3+})$, $x = t_e(O^{2+})$, and $w = t_e(C^{2+})$. We use the relations above to estimate the temperatures needed to infer the carbon ionic abundances.

Regarding the ICF for the carbon, Garnett et al. (1995a), by using photoionization models simulating H II regions, proposed (see also Berg et al. 2016; Skillman et al. 2020) that $({\rm C/O}) = {\rm ICF}({\rm C^{2+}/O^{2+}}) \times ({\rm C^{2+}/O^{+2}})$, where ${\rm ICF(C^{2+}/O^{2+})} = ({\rm O^{2+}/O})/({\rm C^{2+}/C})$. However, we aim to estimate C/H; therefore, a distinct approach is required. We followed the approach performed by Ji et al. (2024), in which the carbon ICF was obtained by comparing the results of photoionization models with observational line intensity ratios. In Fig. 4, a $\log(C43)$ versus log(C III]/C IV) diagram containing the observational data of our sample (red triangles) are compared to the model results (circles). The colour bar indicates the metallicity (in relation to solar) of the models, and the arrow indicates the direction in which the ionization parameter increases. To derive the carbon ICF for the objects for which it was possible to apply the T_e-method (see Table 4), we adopted the following methodology.

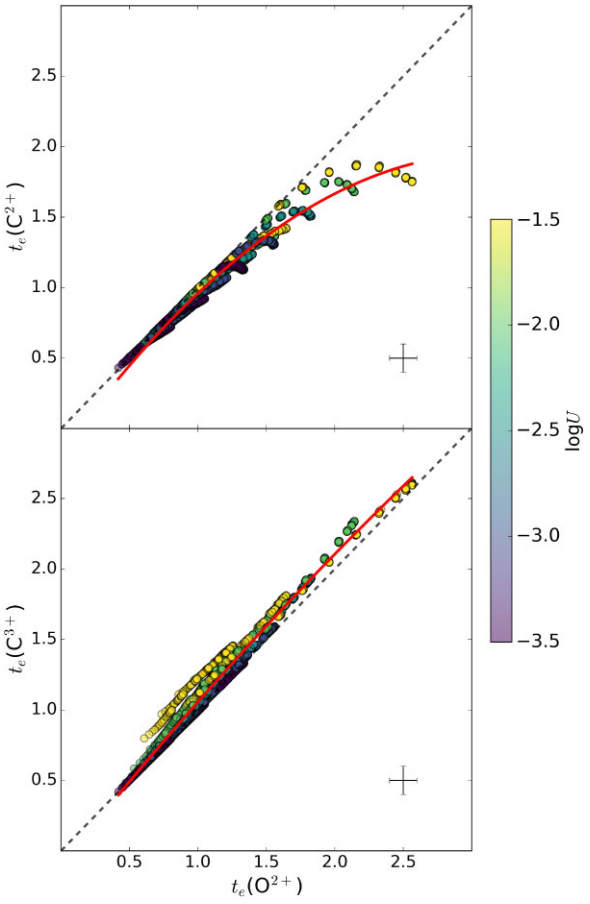

Figure 3. Comparisons between different electron temperature values predicted by our photoionization model results (see Section 2.2) simulating NLRs. The values correspond to the model-predicted mean temperature (in units of 10^4 K) for each ion over the nebular AGN radius times the electron density. The dashed line corresponds to the equality between the temperatures. The error bars represent the typical temperature uncertainty of ±1000 K (e.g. Dors et al. 2023). The colour bar represents the logarithm of the ionization parameter [$\log U$] assumed in the photoionization models. Bottom panel: $t_e(C^{3+})$ versus $t_e(O^{2+})$. The red line represents a fitting to the points given by equation (24). Top panel: $t_e(C^{2+})$ versus $t_e(O^{2+})$. The red line represents a fitting to the points given by equation (25).

(i) First, from the comparison in Fig. 4, we selected a model that better represents a given object assuming the minimal value of χ^2, being

$$\chi^2 = [(C43)_{\rm mod.} - (C43)_{\rm obs.}]^2 + [(C3C4)_{\rm mod.} - (C3C4)_{\rm obs.}]^2, \quad (26)$$

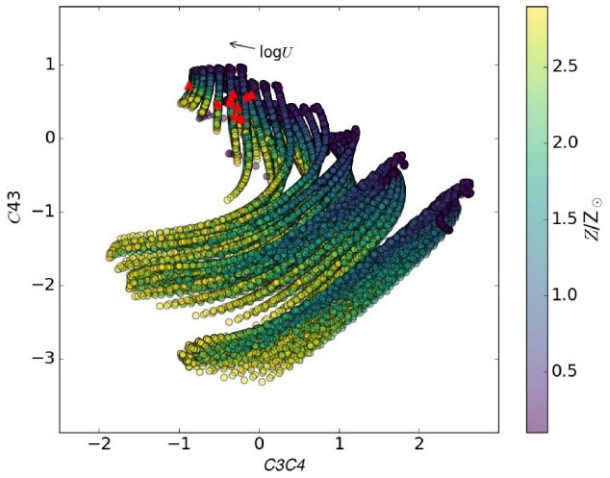

Figure 4. $C43$ = log[(C IV]λ1549 + C III]λ1909)/He IIλ1640] versus $C3C4$ = log[C III]λ1909/C IV]λ1549]. The circles represent the results of our photoionization models (see Section 2.2), and the red triangles represent the observational data of our sample (see Section 2.1). The colour bar indicates the metallicity (in relation to the solar one) assumed in the models. The arrow indicates the direction in which the ionization parameter assumed in the models increases.

where the 'mod.' and 'obs.' indexes represent the model-predicted and observational line ratio, respectively.

(ii) After the model selection, we consider the predicted ionic abundances calculated over the nebular radius times electron density. Thus, the ICF is derived by

$$\mathrm{ICF}(C^{2+}+C^{3+}) = \frac{C}{C^{2+}+C^{3+}}. \quad (27)$$

We derive the carbon ICF that ranges from ~ 1.3 to ~ 2.5, as listed in Table 4. Furthermore, we verify the dependence of the (C/H)–Z relation on the ICF estimations. With this aim, we run two new grids of photoionization models (not shown): one assuming a fixed value of $\log(C/O)_{\odot} = -0.30$, and another using the relation (equation 13) proposed by Nicholls et al. (2017). We find almost the same ICF values as those derived from our grid (see Section 2.2), assuming the (C/H)–Z relation (equation 5 proposed by Dopita et al. (2006). For a detailed discussion on how uncertainties in ICFs can affect C/O estimates see, for instance, Gutkin et al. (2016).

The values adopted as references for the oxygen and carbon abundances are the solar ones: $\log(O/H)_{\odot} = -3.31$ and $\log(C/H)_{\odot} = -3.61$ derived by Allende Prieto, Lambert & Asplund (2001) and Allende Prieto, Lambert & Asplund (2002), respectively. As usual, we use metallicity (Z) and oxygen abundance [12 + log (O/H)] interchangeably (see Nicholls et al. 2017 and Kewley, Nicholls &

Table 4. Physical parameters for our sample. $T_{O^{2+}}$ is the electron temperature calculated directly from the observational value of the [O III](λ4959 + λ5007)/λ4363 by using the PYNEB code. $T_{C^{3+}}$ and $T_{C^{2+}}$ are temperatures calculated from the theoretical relations given by the equations (24) and (25), respectively, while $T_{O^{+}}$ from equation (16). Ionic abundances are derived as described in Section 2.4. The electron density is derived from the [S II]λ6716/λ6731 by using the PYNEB code. ICFs and total abundance values are estimated as described in Section 2.4. Metallicity ($Z/Z_{\odot}$) values are estimated through distinct methods, according to the following sub-indexes: $D20$ via T_e-method (Dors et al. 2020b); $D19$ via the calibration by Dors et al. (2019); $D21$ via the calibration by Dors (2021); $C20$ via the semi-empirical calibration by Carvalho et al. (2020). $O32$ and $C3C4$ correspond to [O III]λ5007/[O II]λ3727 and [C III]λ1909/[C IV]λ1549 line ratios, respectively, used to estimate the logarithm of the ionization parameters through the calibrations proposed by $C20$, $Z24$, and $D19$. The error in Z estimates is attributed to be 50 per cent and in log U estimates 0.15 dex (see Section 2.3).

	NGC 5506	NGC 1068	NGC 7674	NGC 4507	Mrk 3	Mrk 573	Mrk 1388	MCG-3-34-64	III Zw77	4C + 40.36	4C + 23.56
$T_{C^{3+}}$	14 567	14 719	12 004	23 174	15 743	14 188	–	17 400	–	–	–
$T_{C^{2+}}$	12 694	12 803	10 757	17 633	13 516	12 420	–	14 600	–	–	–
$T_{O^{2+}}$	13 692	13 835	11 310	22 157	14 804	13 336	–	16 394	–	–	–
$T_{O^{+}}$	7834	5804	8884	8527	9314	9307	–	9368	–	–	–
N_e (cm^{-3})	1115	25 025	1324	1030	1098	910	348	1350	712	–	–
$\log(O^{+}/H^{+})$	−3.81	−3.54	−4.00	−3.60	−3.70	−3.77	–	−3.78	–	–	–
$\log(O^{2+}/H^{+})$	−4.03	−3.78	−3.53	−4.39	−3.85	−3.75	–	−4.01	–	–	–
$\log(He^{+}/H^{+})$	−1.11	−1.01	–	–	−1.25	−1.15	–	−0.90	–	–	–
$\log(He^{2+}/H^{+})$	−1.86	−1.44	−1.64	−1.80	−1.80	−1.51	–	−1.30	–	–	–
$\log(C^{2+}/He^{2+})$	−1.77	−1.94	−1.33	−3.01	−2.21	−2.11	–	−2.61	–	–	–
$\log(C^{3+}/He^{2+})$	−2.60	−2.55	−1.87	−4.34	−2.88	−2.49	–	−3.49	–	–	–
$\log(C^{2+}/H^{+})$	−3.63	−3.38	−2.97	−4.81	−4.01	−3.62	–	−3.91	–	–	–
$\log(C^{3+}/H^{+})$	−4.46	−3.99	−3.51	−6.14	−4.68	−4.00	–	−4.79	–	–	–
ICF(O)	1.17	1.37	1.50*	1.50*	1.27	1.43	–	1.37	–	–	–
ICF(C)	2.50	2.27	1.50	1.30	2.08	1.85	–	1.75	–	–	–
12 + log(O/H)	8.46	8.79	8.76	8.63	8.63	8.69	–	8.55	–	–	–
$12+\log(C/H)_{\text{equation 33}}$	8.82	9.06	9.31	7.32	8.38	8.79	–	8.38	–	–	–
$\log(C/O)_{\text{equation 33}}$	0.36	0.27	0.55	−1.31	−0.25	0.10	–	−0.17	–	–	–
						Metallicity					
$Z/Z_{\odot}(T_e)_{D20}$	0.59	1.26	1.17	0.83	0.83	1.00	–	0.72	–	–	–
$Z/Z_{\odot}(C43)_{D19}$	0.47	0.70	0.54	0.97	1.01	1.67	1.11	1.69	1.50	1.11	1.77
$Z/Z_{\odot}(R_{23})_{D21}$	0.57	0.65	0.67	0.66	1.03	0.88	0.49	0.81	–	1.02	0.68
$Z/Z_{\odot}(N2)_{C20}$	0.88	1.34	0.92	0.62	0.94	0.82	0.44	1.42	0.09	1.25	0.32
						Ionization parameter					
$\log U\ (O32)_{C20}$	−2.45	−1.17	−1.22	−2.28	−2.19	−2.06	−0.86	−2.05	−1.45	−2.48	−2.15
$\log U\ (O32)_{Z24}$	−2.58	−1.61	−1.66	−2.48	−2.40	−2.31	−1.44	−2.29	−2.04	−2.59	−2.44
$\log U\ (C3C4)_{D19}$	−1.69	−1.44	−1.62	−1.41	−1.41	−1.26	−1.41	−1.47	−0.93	−1.51	−1.52
$\log U\ (C3C4)_{Z24}$	−2.07	−1.77	−1.98	−1.69	−1.69	−1.44	−1.68	−1.66	−1.00	−1.77	−1.70

Sutherland 2019 for a discussion), being its relation

$$12 + \log(\mathrm{O/H}) = 12 + \log[(Z/\mathrm{Z}_{\odot}) \times 10^{-3.31}]. \quad (28)$$

Since most of the objects in our sample do not have errors in the compiled emission lines, we adopted a typical error of 10 per cent for strong emission lines (e.g. [O III]λ5007) and 20 per cent for auroral lines (e.g. [O III]λ4363), such as derived by Kraemer et al. (1994). This translates into an uncertainty of ~ 0.1 dex in the abundance values.

For 4/11 objects of our sample is not possible to apply the T_e-method either because no auroral lines were measured (4C+40.36 and 4C + 23.56) or due to the $RO3 = [\mathrm{O\,III}](\lambda4959 + \lambda5007)/\lambda4363$ line ratio being out of the validity range of its relation with the electron temperature (III Zw77 and Mrk 1388) indicating temperatures higher than 25 000 K.

3 RESULTS AND DISCUSSION

3.1 Metallicity discrepancy

It seems that the first metallicity estimate for NLRs through UV lines was carried out by Nagao et al. (2006), who derived subsolar metallicity values [$0.2 \lesssim (Z/Z_{\odot}) \lesssim 1.0$] for selected quasars ($1.5 \leq z \leq 3.7$) by comparing narrow observational UV line intensity ratios with photoionization model results and assuming that they are mainly emitted by low-density gas clouds ($N_e \leq 10^3$ cm^{-3}). Also, Nagao et al. (2006) did not find any evidence of the evolution of the gas metallicity in the NLRs within their studied redshift range[4] (see also Jiang et al. 2007; Matsuoka et al. 2009; De Rosa et al. 2014; Xu et al. 2018; Tang et al. 2019; Onoue et al. 2020). This result implies that the main epoch of star formation in the host galaxies of AGNs likely occurred at $z > 4$. Recent estimates of the metallicity of AGNs at $z > 6$, mainly based on UV lines, have yielded not-expected high values, around 0.3 times the solar metallicity (e.g. Schmidt et al. 2021; D'Antona et al. 2023; Isobe et al. 2023; Castellano et al. 2024; Ji et al. 2024; Rizzuti et al. 2024), supporting the result obtained by Nagao et al. (2006), in which AGNs reach their chemical maturity in the early epoch of the Universe.

Another important result concerns the relation between AGN metallicity (Z_{AGN}) and the mass of the host stellar galaxy mass ($M_{\star}$). From UV emission lines, Dors et al. (2019) found a clear trend for this relation, showing that Z_{AGN} increases with $M_{\star}$ for objects within the $0 < z < 3.8$ range. It is worth to be mentioned that this result is not observed for most local ($z < 0.4$) active nuclei with Z_{AGN} estimates via optical lines (e.g. Dors et al. 2020a; Li et al. 2024; Oliveira et al. 2024). Since the optical and UV metallicity estimates in the literature have been conducted for galaxies within a similar mass range ($10^{9.5} \lesssim [M_{\star}/\mathrm{M}_{\odot}) \lesssim 10^{12}$], although for distinct observational samples, the inconsistency in the Z_{AGN}–$M_{\star}$ relation described above does raise questions about the reliability of Z_{AGN} estimates across different wavelength ranges.

The main goal of this study is to investigate the discrepancy between the metallicity of NLRs derived through UV and optical emission lines. In particular, we focus our analysis on UV metallicities based on carbon lines, specifically, from the $C43$ index, suggested by Dors et al. (2014) as a metallicity tracer. This line ratio, in principle, is a more reliable Z tracer than other indexes based on lines emitted by only an ion (e.g. O III]λ1666/He IIλ1640, see Zhu et al. 2024) because it involves lines emitted by ions with distinct ionization stages that occupy a large region along the nebular radius, similar to the R_{23} index largely used in optical Z estimates (Pagel et al. 1979).

We start our analysis by comparing metallicity estimates for our sample (see Table 1) via the $C43 - Z$ relations derived by Dors et al. (2019, equation 6) with those from the T_e-method (see Section 2.4). This comparison is shown in the bottom part of the panel (a) of Fig. 5, where the line represents the equality between the Z values. In the top part of the panel (a) of Fig. 5, the ratio (ZR = y/x) between the Z estimations, its mean value ($<ZR>$), a linear fitting (in red) to the points, and a line representing $ZR = 1$ are presented. It can be noted that, although the analysis is feasible for a few objects (for which the T_e-method could be applied) presenting a large dispersion, a clear negative trend for ZR arises. The mean value derived for the metallicity ratio ($<ZR>$) is close to one and $C43$ tends to produce lower Z values than those via the T_e-method for $(Z/\mathrm{Z}_{\odot}) \gtrsim 1$, while an opposite behaviour is observed for $(Z/\mathrm{Z}_{\odot}) \lesssim 1$.

Since for this study we were only able to compile from the literature a reduced sample of objects with the required observational data, and it was not possible to apply the T_e-method for all of them (only on 7/11 objects), we consider as a reference method the empirical $R_{23} - Z$ calibration (equation 10) proposed by Dors (2021). Comparison between Z estimates via the $C43$ index and that via the R_{23} is shown in panel (b) of Fig. 5. For III Zw77 was not possible to estimate Z via R_{23} because its line ratio intensities are out of the validity of the metallicity calibrations assumed. Fig. 5 shows that metallicity values from the $C43$ calibration by Dors et al. (2019) overpredicts Z by a mean factor $<ZR>\sim 1.5$. As in the case of the comparison with the results obtained through the T_e-method, there is a similar trend of Z estimates via $C43$ and R_{23}.

The Z estimates from the R_{23} calibration and the T_e-method are independent of any carbon–oxygen relation, as any other calibration not involving carbon emission lines. This is evidenced by the similar behaviour (see Fig. 5) of the ZR ratio between estimates via $C43$ and those from T_e-method and R_{23} as well as their similar negative trend. As an additional test of this hypothesis, in Fig. 6, Z values derived from the $C43$ calibration proposed by Dors et al. (2019) are compared with those from the $N2$ calibrations proposed by Carvalho et al. (2020). Again, the same negative trend is noted. The behaviour shown by these comparisons indicates that the results in Figs 5 and 6 could be attributed mainly to the assumption of an unrealistic (C/O)–(O/H) abundance relation in the models, rather than to other nebular parameters (e.g. SED or dust content).

3.2 Discrepancy source

To investigate the source of the discrepancy in Z derived from UV and optical emission lines, we analysed the dependence of the ratio (ZR) between Z estimates obtained using the $C43$ and R_{23} calibrations (see Fig. 5) on some nebular parameters. This analysis was necessary due to the limited number (7/11) of direct metallicity estimates available for our sample.

In Fig. 7, the logarithm of the ionization parameter ($\log U$) for our sample (see Table 4) derived through $O32$ (bottom panel) and $C3C4$ (middle panel) as well as the electron density (N_e; top panel) are plotted against the ratio (ZR) between Z estimates via $C43$ and R_{23}. Values of $\log U$ estimated from $O32$ and $C3C4$ are derived by using the Carvalho et al. (2020) and Dors et al. (2019) calibrations (see equations 12 and 7, respectively), while Z_{C43} through the semi-empirical calibration (equation 6) by Dors et al. (2019). The linear fittings (coefficients not shown) and their corresponding Pearson correlation coefficient values (R) are shown in Fig. 7. It was found

[4]For an opposite result for local ($z < 0.5$) AGNs see Carr et al. (2023).

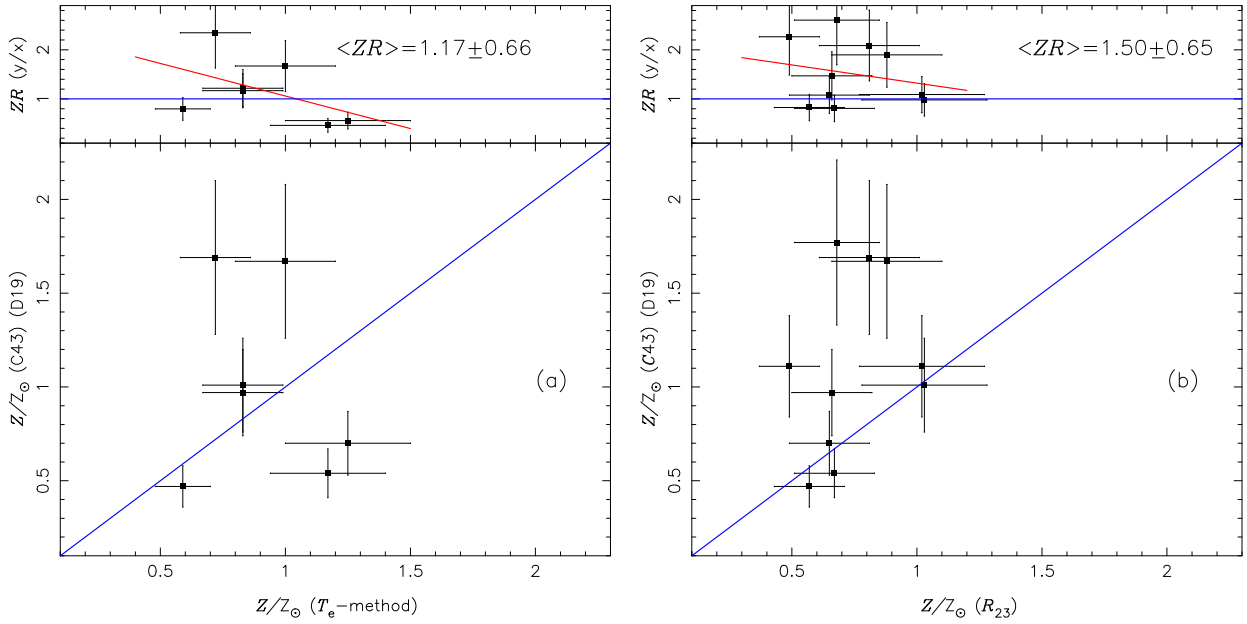

Figure 5. Bottom parts of panels: comparison between metallicity Z (in relation to $Z_{\odot}$) derived using the methods described in Section 2.3. The lines represent the equality between the estimates. The points represent Z estimates for our sample of objects (see Table 4). The y-axes represent estimates obtained assuming UV emission-line ratios and $C43$–Z calibrations, where D19 refers to estimates from the semi-empirical calibration by Dors et al. (2019, lower panels). The x-axes represent estimates through the T_e-method (Dors et al. 2020b, left panels) and the empirical R_{23}-Z calibration proposed by Dors (2021, right panels) using optical lines. Top parts of panels: ratio (ZR = y/x) between the estimates. The blue lines represent the ratio $ZR = 1$, and red lines represent linear fittings to the points (coefficients not shown).

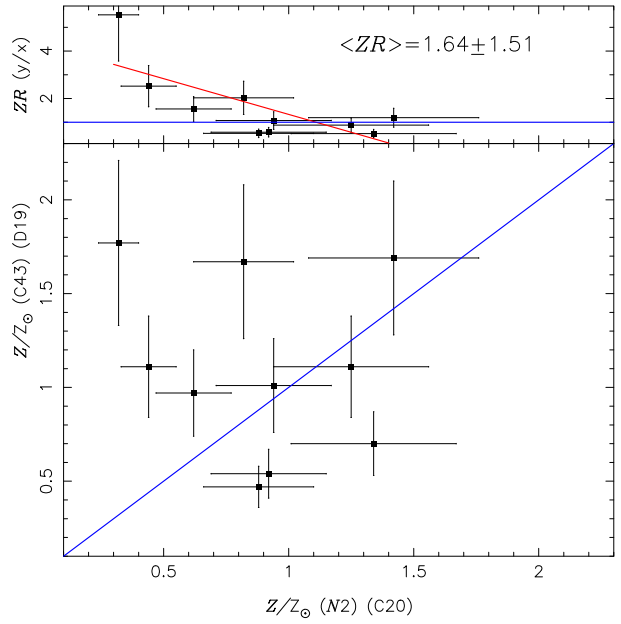

Figure 6. As Fig. 5 but assuming Z estimates via $N2$-Z calibrations in the x-axis, being $N2 = [\mathrm{N\,II}]\lambda6584/\mathrm{H}\alpha$. C20 refers to semi-empirical calibration by Carvalho et al. (2020).

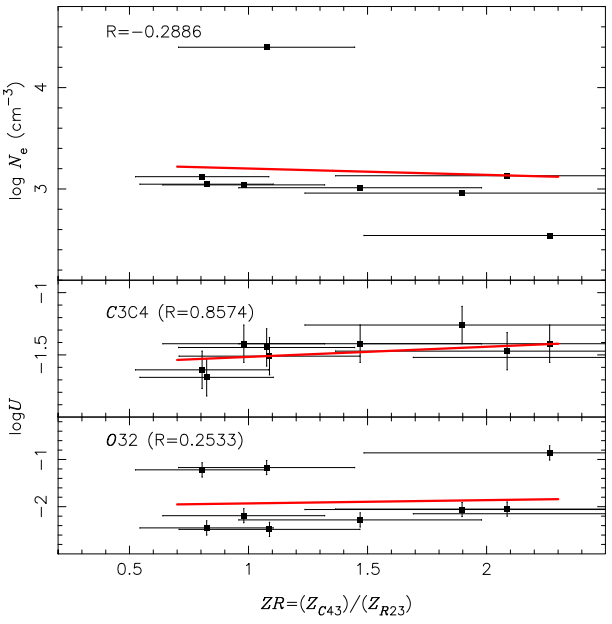

Figure 7. Logarithm of the ionization parameter ($\log U$; bottom and middle panels) and of the electron density ($\log N_e$; top panel) versus the ratio between the metallicity (ZR) derived by using the $C43$ and R_{23} indexes. In the bottom panel, $\log U$ was estimated via the $O32$ and using equation (12) proposed by Carvalho et al. (2020). In the middle panel, $\log U$ was estimated via the $C3C4$ and using equation (7) by Dors et al. (2019). Z_{C43} represents the metallicity estimated by using the calibrations by Dors et al. (2019), while Z_{R23} by using the calibration by Dors (2021). In each panel, the red line represents a linear fitting (coefficients not shown) to the points and its corresponding value for the Pearson correlation coefficient R is indicated.

that the R value indicates a weak correlation between ZR and $\log U$ via $O32$. However, when $\log U$ is derived through $C3C4$, the R values indicate a moderate correlation with ZR. These distinct results could be an indication that these emission-line ratios ($O32$ and $C3C4$) trace the ionization degree of different gas regions in NLRs of AGNs, influencing the Z estimates. This is because both $C43$ and R_{23} calibrations take into account the ionization degree of

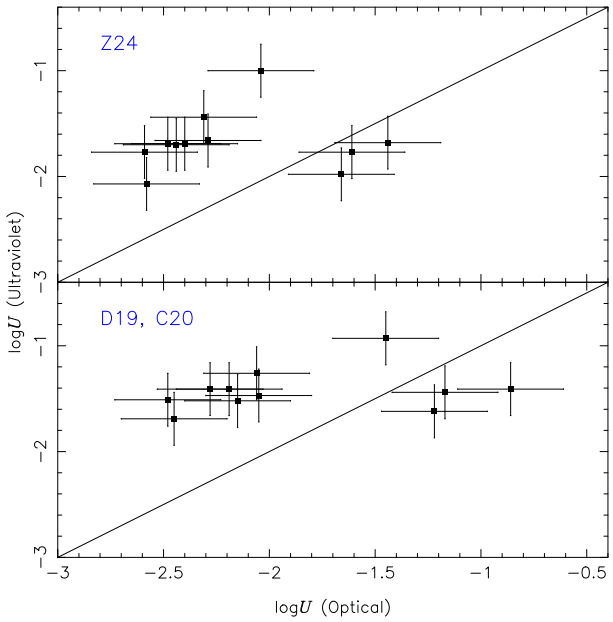

Figure 8. Logarithm of the ionization parameter (log U) derived from $C3C4$ versus those via $O32$. Bottom panel: the calibrations proposed by Carvalho et al. (2020) and Dors et al. (2019) were used to derive log U, while in the top panel the calibrations proposed by Zhu et al. (2024) were used. The lines indicate the equality between the estimates.

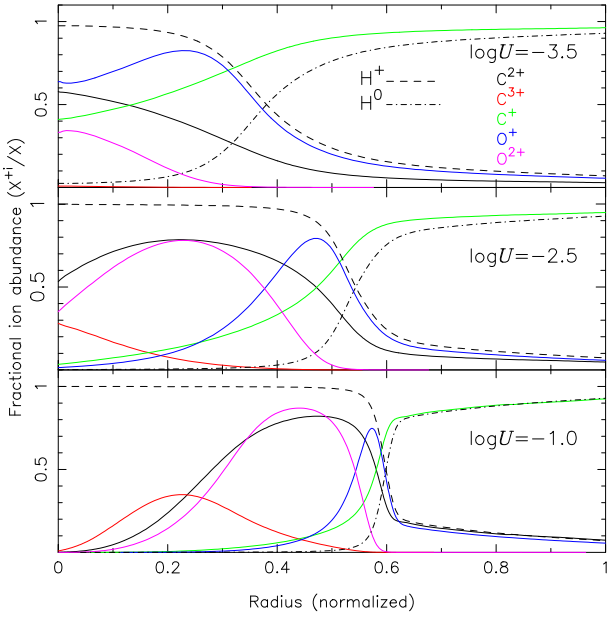

Figure 9. Ionic abundance fraction for distinct ions (X^i/X) versus the nebular radius (normalized by the outermost radius) predicted by photoionization models simulating NLRs of AGNs. The nebular parameters assumed in the models are spherical geometry, solar metallicity, $\alpha_{ox} = -1.1$, and three values for the log $U = -1.0$, -2.5, and -3.5, as indicated.

the gas via $C3C4$ and $O32$, respectively, i.e. they are bi-parametric calibrations (see Zhu et al. 2024 and references therein).

The moderate correlation between log U via $C3C4$ and ZR could be attributed, in part, to the C^{3+} ion being concentrated in inner/denser layers with a higher ionization degree and, probably, with distinct abundances than outer regions containing most of the O^+ and O^{2+} ions. Indeed, optical spatially resolved gas-phase metallicity estimates in local ($z \lesssim 0.013$) Seyfert galaxies by Armah et al. (2024) show an increase of O/H (~ 0.2 dex) and a decrease of N_e (by a factor of ~ 3) with the increase of the nebular radius for most of the objects analysed (see also Revalski et al. 2018). Moreover, analysis of a large sample of 80 quasars at $z \sim 3$ by Guo et al. (2020) shows a radial decline of the flux of the C IVλ1549 and He IIλ1640 emission lines, indicating a variation of abundances and/or ionization degree with the nebular radius. Thus, the ZR discrepancy could be interpreted as a result of metallicities derived from UV emission lines (specifically the $C43$) are representative of inner gas regions of AGNs, while the R_{23} of outer layers. If this supposition is correct, we could derive a correlation between $ZR = Z_{C43}/Z_{R_{23}}$ and the electron density. In Fig. 7, top panel, the logarithm of the electron density (in cm^{-3}) versus ZR is shown. Although the linear fitting indicates a correlation, the Pearson correlation coefficient value (R) shows that it is weak. The electron density was derived from the [S II]λ6716/λ6731 line ratio, which traces the density in outer layers with low abundance of C^{3+}, i.e. the N_e values shown in Fig. 7 are not representative for the gas region where most of this ion is concentrated. Electron density estimates via lines emitted by ions with higher ionization potential values than for S^+ (e.g. [Ar IV]λ4711/λ4740; see Congiu et al. 2017; Cerqueira-Campos et al. 2021; Holden et al. 2023; Binette et al. 2024) are needed to improve the above analysis. In any case, the assumption that $C3C4$ traces the ionization degree of inner layers than the $O32$ is supported by the lower U values derived from the latter. To show that, in Fig. 8, the log U values derived from $C3C4$ are compared with those via $O32$ for our sample (listed in Table 4), where the calibrations by Zhu et al. (2024) are also included. It can be seen that for most of the cases and independently of the calibrations assumed, $C3C4$ yields higher U values than $O32$.

As an additional test to verify if the $C43$ and R_{23} indexes trace the metallicity of distinct gas regions in AGNs, we build photoionization models to analyse the ionization structure of the carbon and oxygen. We assume as nebular parameters a spherical geometry, solar metallicity, $\alpha_{ox} = -1.1$, and three values for log U: -1.0, -2.5, and -3.5 dex. These parameter values are typical of NLRs (e.g. Pérez-Montero et al. 2019). In Fig. 9, the resulting ionization structure for the carbon (C^+, C^{2+}, C^{3+}), oxygen (O^+, O^{2+}), and hydrogen (H^0, H^+) is shown. We can note the following:

(i) Independently of the value assumed for log U, C^{2+} and O^{2+} occupy similar gas regions. This result shows the reliability of C/O abundance estimates for AGNs via the C III]/O III] line ratio.

(ii) C^{3+} and O^+ are concentrated preferably in inner and outer layers, respectively, independently of the log U assumed. Thus, for AGNs with radial abundance profiles, naturally, $C43$ and R_{23} indexes tend to represent the metallicity of distinct gas regions. In any case, any calibration must be applied by assuming emission-line ratios measured from integrated spectra, in which the influence of radial abundance profiles on Z estimates is minimized. Thus, the discrepancy ZR observed in this study, probably, is not due to the C^{3+} and O^+ ions being concentrated in distinct gas regions.

(iii) C^+ extends into the neutral hydrogen zone, being its fraction in the ionized region about null for log $U = -1.0$. This result makes it incorrect to use C^+ in the C/H abundance estimates.

Similar results are also derived for H II regions, as shown by Berg et al. (2019), who built photoionization models simulating H II regions to reproduce the C^{3+}/C^{2+} ionic abundance ratio. In their models, it was necessary to require high ionization parameters (log $U \sim -1.5$), being the typical values for H II regions derived

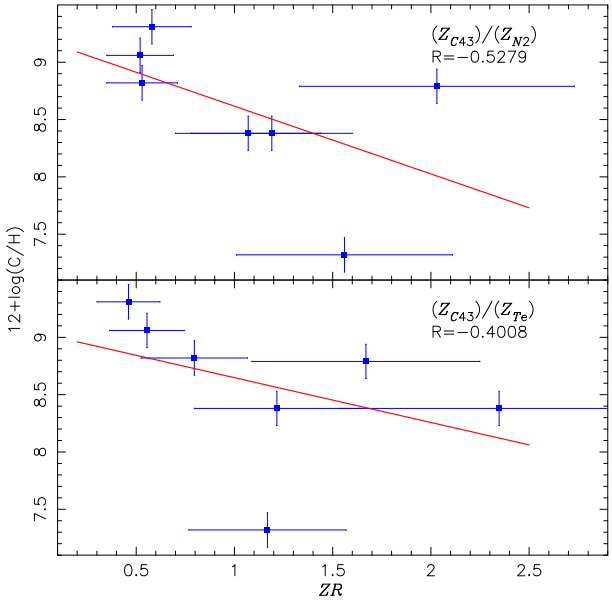

Figure 10. Carbon abundance [in units of 12 + log(C/H)] versus the ratio (ZR) between the metallicity derived through the $C43$ index and T_e-method (lower panel) and $N2$ index (upper panel). The points represent the estimates for our AGN sample, while the lines are the linear fittings (coefficients not shown) to them.

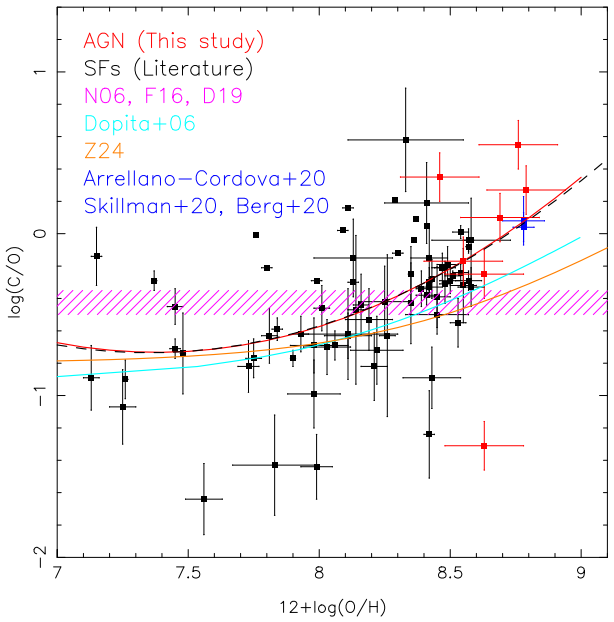

Figure 11. Logarithm of the C/O abundance ratio versus the oxygen abundance [in units of 12 + log(O/H)]. The red points represent the estimates for our AGN sample (see Table 4). The black points represent SF estimates derived by Walter, Dufour & Hester (1992), Garnett et al. (1999), Esteban et al. (2009, 2014), Berg et al. (2016), Peña-Guerrero et al. (2017), Skillman et al. (2020), and Arellano-Córdova et al. (2020). The blue points represent the extrapolations to the nuclear region (galactocentric distance equal to 0) of the radial abundance gradients derived for the MW by Arellano-Córdova et al. (2020) and for M 101 by Skillman et al. (2020) and Berg et al. (2020). The cyan and orange curves represent the abundance relations assumed in photoionization models by Dopita et al. (2006) and Zhu et al. (2024), respectively. The dashed area represents the range $-0.5 \leqq \log(C/O) \leqq -0.35$ assumed in photoionization models by Nagao et al. (2006), Feltre et al. (2016), and Dors et al. (2019). The red curve shows the abundance relation obtained taking into account both AGNs and SFs (Eq.30) and the dashed line is the same but only considering SFs.

from optical lines in order of $\log U \sim -2.5$ (e.g. Dors et al. 2011; Zinchenko et al. 2019; Grasha et al. 2022; Ji & Yan 2022; Garner Ray et al. 2025). The fact that C^+ extends into the neutral zone, in principle, precludes its use in determining the C/H total abundance, as for O^0 in the O/H abundance calculations.

Concerning the carbon influence on discrepancies of the Z estimations via UV and optical lines, in Fig. 10, values of the carbon abundance [in units of 12 + log(C/H)] for our sample of objects versus the ratio (ZR) between metallicity estimates derived through the $C43$ calibration and the T_e-method (lower panel) and the $N2$ calibration (upper panel) are shown. This plot also presents a linear fitting (coefficients not shown) to the points and their corresponding R values. Despite the R values indicating a weak correlation, we can see that ZR increases when the carbon abundance decreases. Since the C/O–O/H abundance relation assumed as the input parameter in photoionization models deeply influences predictions of carbon emission lines, the discrepancy found above can result from incorrect suppositions of this relation in photoionization models. Distinct carbon–oxygen relations have been adopted in metallicity studies of AGNs. Nakajima et al. (2018) built a large grid of photoionization models to derive UV diagnostic diagrams used to classify and obtain nebular parameters of galaxies. These authors investigated models with distinct C/O–O/H relations and found that an enhanced C/O abundance ratio (up to the solar value) is needed for models with metallicities $(Z/Z_\odot) \sim 0.2$ to reproduce UV emission-line ratios of galaxies at $z = 2$–4. The photoionization models used by Dors et al. (2019) to derive the $C43$–Z relation assume a fixed $\log(C/O)_\odot = -0.50$, a similar value assumed in the NLR models of Nagao et al. (2006) and Feltre et al. (2016). Finally, Zhu et al. (2024), opposite to the majority of previous studies that use nebular estimates, assumed in their photoionization models a C/O–O/H abundance relation derived from stellar abundance data in the Milky Way (MW) provided by Nicholls et al. (2017).

Our direct carbon abundance estimates can be used to constraint a more representative (C/O)–Z relation for NLRs of AGNs. However, due to our small sample of objects for which it was possible to estimate C/H (seven objects) and the narrow range of metallicity of them [$0.6 \lesssim (Z/Z_\odot) \lesssim 1.3$[5]], it is desirable to combine our estimates with those for SFs. This practice was adopted in other previous studies dedicated to derive abundance relations of other elements in NLRs of AGNs (e.g. Pérez-Montero et al. 2019, 2023; Armah et al. 2021; Monteiro & Dors 2021; Dors et al. 2022, 2023, 2024b; Peluso et al. 2023) and low-ionization nuclear emission-line region (LINER) galaxies (e.g. Oliveira et al. 2024). Moreover, comparing the relative abundance (e.g. N/O, C/O) of objects of distinct classes yields important information on the stellar evolution and chemical ISM enrichment in different environments. In this regard, in Fig. 11, a plot of log(C/O) versus 12 + log(O/H), our abundance estimates (red points) are plotted together with those for SFs (black points). A dashed area representing the fixed log(C/O) values assumed in previous calibrations is also shown in this figure. The SF abundance estimates, taken from the literature obtained by distinct authors and for local ($z \lesssim 0.2$) objects, are derived either from UV C III]λ1909/O III]λ1666 collisional excited lines or from optical O II and C II recombination lines, both combined with the [O III]λ5007 (e.g. Esteban et al. 2009; Berg et al. 2016). These

[5]Metallicity range derived by assuming the T_e-method (see Table 4).

distinct methodologies to derive abundance can contribute to the scatter of C/O abundances at fixed O/H values. In fact, even in the best case, where the C IIλ4267 and O IIλ4649 recombination lines are measured, the O^{2+} ionic abundance is always derived from optically excited lines (Skillman et al. 2020). In Fig. 11 are also included the following:

(i) The (C/O)–Z relation derived for H II regions by Dopita et al. (2006), which is based on results of local SFs compiled by Garnett et al. (1999):

$$(\mathrm{C/H}) = 6.0 \times 10^{-5} \times (Z/Z_{\odot}) + 2.0 \times 10^{-4} \times (Z/Z_{\odot})^2. \quad (29)$$

(ii) The equation (13) assumed by Zhu et al. (2024) and derived from stellar abundance estimates (Nicholls et al. 2017).

(iii) Values of the nuclear interception (radial distance equal to 0) of [12 + log(O/H); log(C/O)] radial gradients derived for the MW by Arellano-Córdova et al. (2020) and for M 101 by Skillman et al. (2020) and Berg et al. (2020). These values correspond to $[8.78\pm0.08, 0.05\pm0.15]_{\mathrm{MW}}$, and $[8.78\pm0.04, 0.158\pm0.09]_{\mathrm{M\,101}}$, and are represented by blue points.

We can note in Fig. 11 that AGNs present similar C/O abundances than the most metallic SFs (mainly composed by inner disc H II regions) and they are in agreement with those from the extrapolation of the radial gradients in the MW and M 101. Also, our small sample of AGNs seem to indicate that, similarly to the (N/O)–(O/H) relation (Dors et al. 2024b), this object class follows the (C/O)–O/H relation for SFs. Only an AGN, i.e. NGC 4507, presents a very low C/O abundance, deviating from the trend shown by AGNs and SFs with similar O/H abundances, although some few SFs are showing a similar deviation. A fitting considering all the points (AGNs + SFs) results in

$$\log(\mathrm{C/O}) = 0.41(\pm0.24)\,\mathrm{x}^2 - 6.07(\pm3.87)\,\mathrm{x} + 21.69(\pm15.45), \quad (30)$$

where $x = 12 + \log(\mathrm{O/H})$. This relation is represented in Fig. 11 by a red curve. We also produced a fitting considering only SF estimates and found the same relation (represented in Fig. 11 by a dashed black line) as that assuming AGNs + SFs. It is worth noting that our relation results in the following:

(i) Values of log(C/O) higher by ~ 0.2 dex than those from the Dopita et al. (2006) and Zhu et al. (2024) relations, while this difference reaches up to ~ 0.4 dex in the region occupied by the AGNs.

(ii) Similar abundances to those derived from nuclear extrapolations of radial abundance gradients in the MW and M 101.

(iii) The fixed values of log(C/O) ~ -0.4, assumed in the photoionization models by Nagao et al. (2006), Feltre et al. (2016), and Dors et al. (2019), do not seem to be representative for NLRs.

To test if the use of our (C/O)–(O/H) abundance relation alleviates the ZR discrepancy derived when metallicities from UV lines are compared with those via optical lines (see Fig. 5), we build a new photoionization model grid by assuming as input parameter the (C/O)–(O/H) relation represented by equation (30). After comparing model results with our observational data, we derive new values of Z_{C43} for each object in our sample from interpolation between the models. This methodology is considered to derive semi-empirical calibrations (e.g. Castro et al. 2017). In a subsequent paper (Dors et al., in preparation), we will produce a new $C43$-Z calibration by assuming abundances from the equation (30), a wide range of nebular parameters (e.g. α_{ox}, N_e), and a large sample of observational data. This study is limited to only analyse the influence of nebular parameters on Z estimates via the $C43$ index calibration.

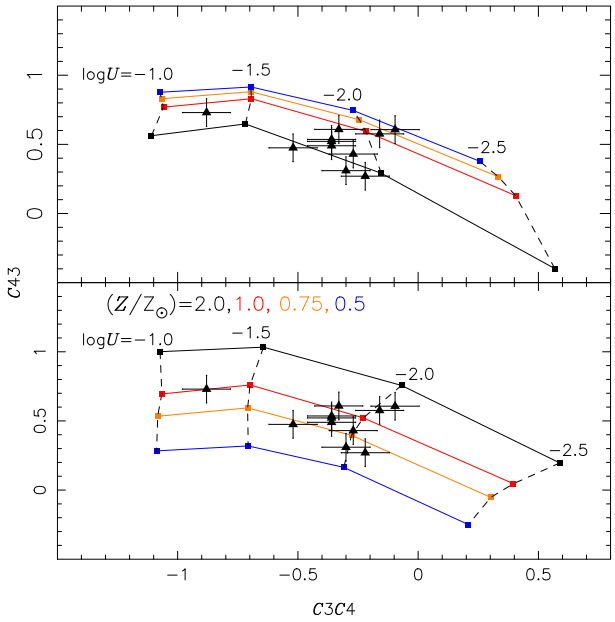

Figure 12. $C43$ = log[(C IV]λ1549 + C III]λ1909)/He IIλ1640] versus $C3C4$ = log[C III]λ1909/C IV]λ1549]. Lower panel: the lines connect the results of photoionization models built assuming the (C/O)–(O/H) abundance ratio given by equation (30). The solid and dashed lines connect model results with the same metallicity and log U, respectively, as indicated. The triangles represent our observational sample. Upper panel: same as the lower panel but for photoionization models assuming a fixed value of $\log(\mathrm{C/O})_{\odot} = -0.30$ (see Section 3.3).

In the lower panel of Fig. 12, a $C43$ versus $C3C4$ diagram, our observational data are compared with the results of our new photoionization model grid. In the bottom part of Fig. 13, we compare the Z values obtained from Fig. 12, lower panel, with those derived using the T_e-method (listed in Table 4) for the objects in our sample for which this comparison is possible. There can be seen a good agreement between the estimates, being NGC 5506 the only object presenting a large disagreement between the estimates. In the top part of Fig. 13, the metallicity ratio ZR versus the metallicity estimates via the T_e-method is shown. The black line represents a linear fitting (coefficients not shown) to all points. As found when the $C43$ calibrations were considered (see Fig. 5), a correlation between ZR and Z_{Te} remains (R ~ -0.6), with the mean value for the metallicity ratio equal to $<ZR>= 1.22 \pm 0.69$. However, excluding estimates for NGC 5506, a new linear fitting (red line) indicates a one-by-one metallicity correlation, with R ~ 0 and $<ZR>= 0.96 \pm 0.16$.

We emphasize that although there is a clear need for a larger number of metallicity estimates via UV lines and the T_e-method to improve the Z comparison, the result in Fig. 13 indicates an agreement between UV estimates and those via the T_e-method. Thus, we argue that the relation between carbon and oxygen abundances is the main source of discrepancy between metallicities based on carbon UV lines and those derived by direct estimates adopting optical emission lines.

3.3 Influence of (C/O)–Z relations

Since some previous UV calibrations (e.g. Dors et al. 2019) have assumed fixed C/O values in their photoionization models, it is helpful to analyse how Z and U derived in this case differ from those obtained through models that assume a more realistic abundance

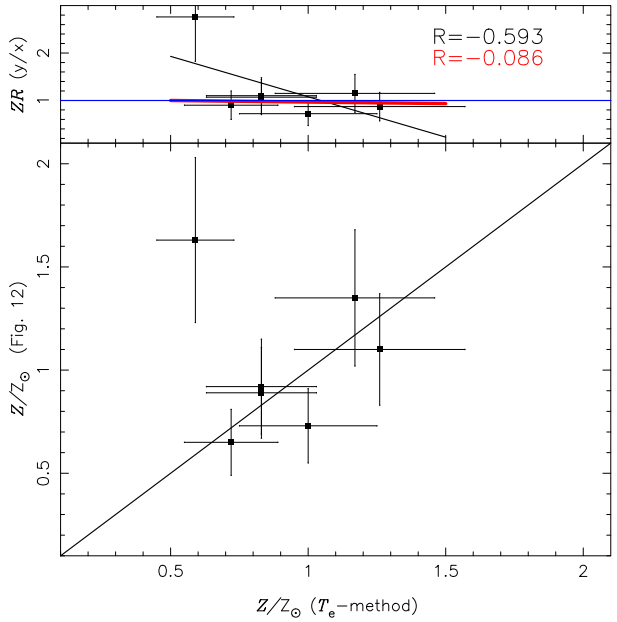

Figure 13. Same as Fig. 5 (left panel) but for metallicities (in relation to the solar one) derived from the interpolation of the models in the lower panel of Fig. 12 versus those via the T_e-method. The black line represents a linear fitting to all points, whose Pearson correlation coefficient (R) is indicated. The red line is like the black one but obtained excluding the outlier NGC 5576 (see the text). The resulting R-value of this fitting is indicated in red.

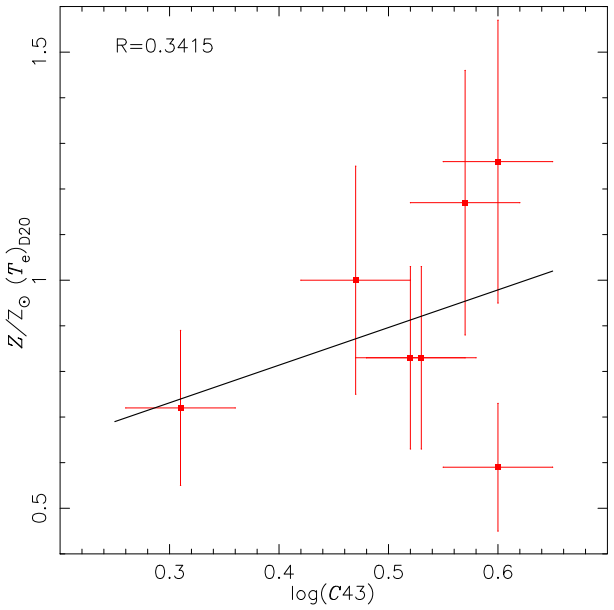

Figure 14. Metallicity (Z), relative to the solar value, calculated through the T_e-method using O/H abundances, is plotted against the observational $C43$ values. The red points represent the values for seven Seyfert 2 galaxies ($z < 0.03$) from our sample (see Table 4) for which it was possible to apply the T_e-method. The line represents a fit to the points (coefficients not shown). The Pearson correlation coefficient value (R) is also shown.

relation. For this purpose, we constructed a photoionization model grid assuming a fixed value of $\log(C/O)_\odot = -0.30$. The results of these models are compared with the observational data in the upper panel of Fig. 12. There can be seen a clear difference with the model results (lower panel of Fig. 12) that assume the (C/O)–(O/H) relation represented by equation (30). The assumption that C/O does not vary with metallicity implies that objects with high $C43$ values exhibit the lowest Z values, i.e. $C43 \propto 1/Z$. In contrast, the models assuming the relation represented by equation (30) indicate that objects with high $C43$ values exhibit the highest Z values, i.e. $C43 \propto Z$. The result that $C43$ must increase with Z is confirmed by our direct estimates shown in Fig. 14, where Z values derived through the T_e-method via O/H abundances are plotted against the observational values of $C43$ for our AGN sample. Despite the large scatter of the points, the R value indicates a positive correlation between Z and $C43$, represented by the red line (a linear fit to the points).

The discrepancy above has a deep impact on the Z estimates. To show that, in Fig. 15, a comparison between the Z and U values derived from both grids of models presented in Fig. 12 is shown. The following can be noted: (i) the use of photoionization models assuming the (C/O)–(O/H) relation represented by equation (30) results in higher Z values than those assuming a fixed C/O solar value for the high-metallicity regime and vice versa, and (ii) lower (~ 0.3 dex) $\log U$ values are derived by models assuming the equation (30) instead of a fixed solar C/O value.

4 CONCLUSIONS

Metallicity (Z) estimates of the gas phase of high-z galaxies are mainly derived by calibrations between strong UV emission lines and this nebular parameter. These estimates Z have shown to be discrepant in relation to those via optical emission lines, being the origin of this discrepancy (ZR) poorly defined. To investigate the origin of ZR in NLRs of AGNs, we compiled from the literature spectroscopic observational data in the UV [$1000 < \lambda(\text{Å}) < 2000$] and optical [$3000 < \lambda(\text{Å}) < 7000$] wavelength ranges a sample of 11 objects (nine at $z < 0.4$ and two at $z \sim 2.4$). We estimated the metallicity for each object of this sample adopting a semi-empirical calibration assuming the $C43 = \log[(\text{C IV}\lambda1549 + \text{C III}]\lambda1909)/\text{He II}\lambda1640]$ index as a metallicity tracer. These estimates were compared with those derived through direct electron temperature measurements, i.e. the T_e-method. Also, calibrations based on optical strong lines were considered when it was not possible to apply the T_e-method (four out 11 objects). The source of the discrepancy was investigated in terms of the ionization parameter (U), electron density (N_e), and carbon abundance (C/H) derived through the T_e-method. A comparison of the ionization parameter estimates based on UV and optical emission lines was also carried out. We found the following results:

(i) $C43$ index tends to overestimate the metallicity for $(Z/Z_\odot) \lesssim 1.0$ and underestimate it for higher Z values in comparison to optical estimates.

(ii) Ionization parameter values derived from the $C3C4 = \text{C III}]\lambda1909/\text{C IV}\lambda1549$ line ratio tend to be higher than those derived from $O32 = [\text{O III}]\lambda5007/[\text{O II}]\lambda3727$.

(iii) Photoionization model simulation of the ionization structure of AGNs indicates that the C^{3+} ion is emitted mainly in inner parts of the nebulae, while O^+ in outer parts. This result indicates that $C3C4$ and $O32$ measure the ionization degree of distinct gas regions in AGNs, possibly having some influence on Z estimates via calibrations adopting these line ratios to mitigate the effect of ionization parameter in Z estimates.

(iv) We found a weak correlation of the ratio (ZR) between metallicities via $C43$ and optical lines with the ionization parameter

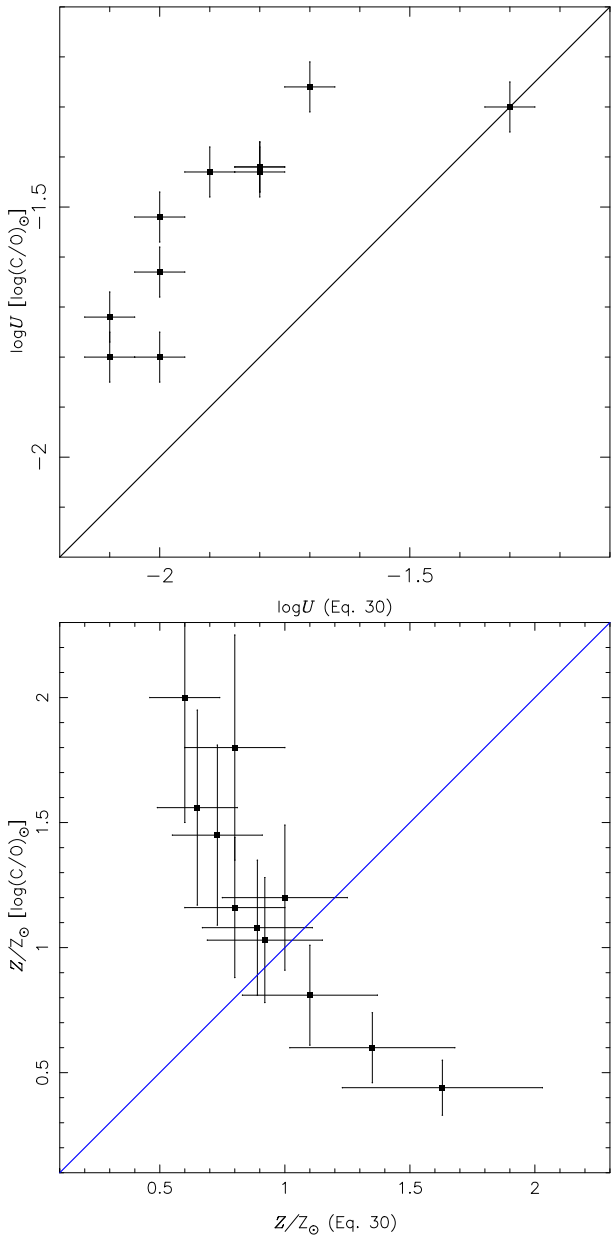

Figure 15. Lower panel: comparison between the metallicity for our AGN sample derived by interpolating the photoionization models (shown in the lower panel of Fig. 12) assuming the (C/O)–(O/H) relation represented by equation (30) versus those from models (shown in the upper panel of Fig. 12) assuming a fixed $\log(C/O)_{\odot} = -0.30$. The line indicates the equality between the estimates. Upper panel: same as the lower panel but for the logarithm of the ionization parameter (U).

and electron density. Otherwise, a moderate correlation was found between ZR and direct estimates of C/H, implying that the (C/O)–Z relations previously adopted in photoionization models for UV carbon-line calibrations might not be accurate for AGNs.

(v) We derived a new (C/O)–Z relation by combining direct abundance estimates from our sample with abundances from a large number of local star-forming objects. Photoionization models based on this new relation yield Z values comparable to those calculated using the T_e-method.

ACKNOWLEDGEMENTS

OLD is grateful to Fundação de Amparo à Pesquisa do Estado de São Paulo (FAPESP), process number 2022/07066-6, and to Conselho Nacional de Desenvolvimento Científico e Tecnológico (CNPq). RAR acknowledges the support from Conselho Nacional de Desenvolvimento Científico e Tecnológico (CNPq; Proj. 303450/2022-3, 403398/2023-1, and 441722/2023-7), Fundação de Amparo à pesquisa do Estado do Rio Grande do Sul (FAPERGS; Proj. 21/2551-0002018-0), and Coordenação de Aperfeiçoamento de Pessoal de Nível Superior (CAPES; Proj. 88887.894973/2023-00). RR acknowledges support from Conselho Nacional de Desenvolvimento Científico e Tecnológico (CNPq; Proj. 311223/2020-6, 304927/2017-1, 400352/2016-8, and 404238/2021-1), Fundação de amparo à pesquisa do Rio Grande do Sul (FAPERGS; Proj. 19/1750-2 and 24/2551-0001282-6), and Coordenação de Aperfeiçoamento de Pessoal de Nível Superior (CAPES; Proj. 0001).

DATA AVAILABILITY

The data underlying this article will be shared on reasonable request to the corresponding author.

REFERENCES

Abazajian K. N. et al., 2009, ApJS, 182, 543
Agostino C. J. et al., 2021, ApJ, 922, 156
Allende Prieto C., Lambert D. L., Asplund M., 2001, ApJ, 556, L63
Allende Prieto C., Lambert D. L., Asplund M., 2002, ApJ, 573, L137
Arellano-Córdova K. Z., Esteban C., García-Rojas J., Méndez-Delgado J. E., 2020, MNRAS, 496, 1051
Arellano-Córdova K. Z. et al., 2022, ApJ, 935, 74
Armah M. et al., 2021, MNRAS, 508, 371
Armah M. et al., 2023, MNRAS, 520, 1687
Armah M. et al., 2024, MNRAS, 534, 2723
Baldwin J. A., Phillips M. M., Terlevich R., 1981, PASP, 93, 5
Baldwin J. A., Hamann F., Korista K. T., Ferland G. J., Dietrich M., Warner C., 2003, ApJ, 583, 649
Berg D. A., Skillman E. D., Henry R. B. C., Erb D. K., Carigi L., 2016, ApJ, 827, 126
Berg D. A., Erb D. K., Henry R. B. C., Skillman E. D., McQuinn K. B. W., 2019, ApJ, 874, 93
Berg D. A., Pogge R. W., Skillman E. D., Croxall K. V., Moustakas J., Rogers N. S. J., Sun J., 2020, ApJ, 893, 96
Berg D. A., Chisholm J., Erb D. K., Skillman E. D., Pogge R. W., Olivier G. M., 2021, ApJ, 922, 170
Berg D. A. et al., 2024, ApJ, 971, 87
Bergeron J., Maccacaro T., Perola C., 1981, A&A, 97, 94
Binette L. et al., 2024, A&A, 684, A53
Bottorff M., Ferland G., Baldwin J., Korista K., 2000, ApJ, 542, 644
Bykov S. D., Gilfanov M. R., Sunyaev R. A., 2024, MNRAS, 527, 1962
Byler N., Kewley L. J., Rigby J. R., Acharyya A., Berg D. A., Bayliss M., Sharon K., 2020, ApJ, 893, 1
Cameron A. J., Katz H., Rey M. P., Saxena A., 2023, MNRAS, 523, 3516
Carr D. J., Salzer J. J., Gronwall C., Williams A. L., 2023, ApJ, 955, 141
Carvalho S. P. et al., 2020, MNRAS, 492, 5675
Castellano M. et al., 2024, ApJ, 972, 143
Castro C. S., Dors O. L., Cardaci M. V., Hägele G. F., 2017, MNRAS, 467, 1507
Cerqueira-Campos F. C., Rodríguez-Ardila A., Riffel R., Marinello M., Prieto A., Dahmer-Hahn L. G., 2021, MNRAS, 500, 2666
Congiu E. et al., 2017, MNRAS, 471, 562
Copetti M. V. F., Mallmann J. A. H., Schmidt A. A., Castañeda H. O., 2000, A&A, 357, 621
D'Agostino J. J. et al., 2019a, MNRAS, 487, 4153

D'Agostino J. J., Kewley L. J., Groves B., Byler N., Sutherland R. S., Nicholls D., Leitherer C., Stanway E. R., 2019b, ApJ, 878, 2
D'Antona F. et al., 2023, A&A, 680, L19
D'Eugenio F. et al., 2024, A&A, 689, A152
Daltabuit E., Cox D., 1972, ApJ, 173, L13
Daltabuit E., MacAlpine G. M., Cox D. P., 1978, ApJ, 219, 372
Davies R. L. et al., 2016, MNRAS, 462, 1616
De Robertis M. M., Hutchings J. B., Pitts R. E., 1988, AJ, 95, 1371
De Rosa G. et al., 2014, ApJ, 790, 145
Denicoló G., Terlevich R., Terlevich E., 2002, MNRAS, 330, 69
Díaz Á. I., Terlevich E., Castellanos M., Hägele G. F., 2007, MNRAS, 382, 251
Dopita M. A., Sutherland R. S., 1996, ApJS, 102, 161
Dopita M. A. et al., 2006, ApJS, 167, 177
Dopita M. A. et al., 2015, ApJS, 217, 12
Dors O. L., 2021, MNRAS, 507, 466
Dors O. L. J., Storchi-Bergmann T., Riffel R. A., Schimdt A. A., 2008, A&A, 482, 59
Dors O. L. J., Krabbe A., Hägele G. F., Pérez-Montero E., 2011, MNRAS, 415, 3616
Dors O. L., Cardaci M. V., Hägele G. F., Krabbe Â. C., 2014, MNRAS, 443, 1291
Dors O. L. J., Arellano-Córdova K. Z., Cardaci M. V., Hägele G. F., 2017, MNRAS, 468, L113
Dors O. L., Agarwal B., Hägele G. F., Cardaci M. V., Rydberg C.-E., Riffel R. A., Oliveira A. S., Krabbe A. C., 2018, MNRAS, 479, 2294
Dors O. L., Monteiro A. F., Cardaci M. V., Hägele G. F., Krabbe A. C., 2019, MNRAS, 486, 5853
Dors O. L. et al., 2020a, MNRAS, 492, 468
Dors O. L., Maiolino R., Cardaci M. V., Hägele G. F., Krabbe A. C., Pérez-Montero E., Armah M., 2020b, MNRAS, 496, 3209
Dors O. L. et al., 2022, MNRAS, 514, 5506
Dors O. L. et al., 2023, MNRAS, 521, 1969
Dors O. L., Cardaci M. V., Hägele G. F., Ilha G. S., Oliveira C. B., Riffel R. A., Riffel R., Krabbe A. C., 2024a, MNRAS, 527, 8193
Dors O. L. et al., 2024b, MNRAS, 534, 3040
Edmunds M. G., 1990, MNRAS, 246, 678
Esteban C., Bresolin F., Peimbert M., García-Rojas J., Peimbert A., Mesa-Delgado A., 2009, ApJ, 700, 654
Esteban C., García-Rojas J., Carigi L., Peimbert M., Bresolin F., López-Sánchez A. R., Mesa-Delgado A., 2014, MNRAS, 443, 624
Feltre A., Charlot S., Gutkin J., 2016, MNRAS, 456, 3354
Ferland G. J., Osterbrock D. E., 1987, ApJ, 318, 145
Ferland G. J. et al., 2017, Rev. Mex. Astron. Astrofis., 53, 385
Flury S. R., Moran E. C., 2020, MNRAS, 496, 2191
Foschini L., 2002, A&A, 385, 62
Garner R., Kennicutt R. J., Rousseau-Nepton L., Olivier G. M., Fernández-Arenas D., Robert C., Martin R. P., Amram P., 2025, ApJ, 978, 70
Garnett D. R., Skillman E. D., Dufour R. J., Peimbert M., Torres-Peimbert S., Terlevich R., Terlevich E., Shields G. A., 1995a, ApJ, 443, 64
Garnett D. R., Dufour R. J., Peimbert M., Torres-Peimbert S., Shields G. A., Skillman E. D., Terlevich E., Terlevich R. J., 1995b, ApJ, 449, L77
Garnett D. R., Shields G. A., Peimbert M., Torres-Peimbert S., Skillman E. D., Dufour R. J., Terlevich E., Terlevich R. J., 1999, ApJ, 513, 168
Grasha K. et al., 2022, ApJ, 929, 118
Groves B. A., Dopita M. A., Sutherland R. S., 2004, ApJS, 153, 75
Groves B. A., Heckman T. M., Kauffmann G., 2006, MNRAS, 371, 1559
Guo Y. et al., 2020, ApJ, 898, 26
Gutkin J., Charlot S., Bruzual G., 2016, MNRAS, 462, 1757
Hägele G. F., Pérez-Montero E., Díaz Á. I., Terlevich E., Terlevich R., 2006, MNRAS, 372, 293
Hägele G. F., Díaz Á. I., Cardaci M. V., Terlevich E., Terlevich R., 2007, MNRAS, 378, 163
Hägele G. F., Díaz Á. I., Terlevich E., Terlevich R., Pérez-Montero E., Cardaci M. V., 2008, MNRAS, 383, 209
Hägele G. F. et al., 2010, MNRAS, 406, 1675
Hamann F., Ferland G., 1992, ApJ, 391, L53
Hirschmann M., Charlot S., Feltre A., Naab T., Somerville R. S., Choi E., 2019, MNRAS, 487, 333
Hirschmann M. et al., 2023, MNRAS, 526, 3610
Holden L. R., Tadhunter C. N., Morganti R., Oosterloo T., 2023, MNRAS, 520, 1848
Humphrey A., 2019, MNRAS, 486, 2102
Humphrey A., Villar-Martín M., Vernet J., Fosbury R., di Serego Alighieri S., Binette L., 2008, MNRAS, 383, 11
Hviding R. E., Hickox R. C., Väisänen P., Ramphul R., Hainline K. N., 2023, AJ, 166, 111
Isobe Y. et al., 2023, ApJ, 959, 100
Izotov Y. I., Thuan T. X., 2008, ApJ, 687, 133
Izotov Y. I., Stasińska G., Meynet G., Guseva N. G., Thuan T. X., 2006, A&A, 448, 955
Jenkins E. B., 2009, ApJ, 700, 1299
Ji X., Yan R., 2020, MNRAS, 499, 5749
Ji X., Yan R., 2022, A&A, 659, A112
Ji X., Yan R., Riffel R., Drory N., Zhang K., 2020, MNRAS, 496, 1262
Ji X. et al., 2024, MNRAS, 535, 881
Jiang L., Fan X., Vestergaard M., Kurk J. D., Walter F., Kelly B. C., Strauss M. A., 2007, AJ, 134, 1150
Kauffmann G. et al., 2003, MNRAS, 346, 1055
Kennicutt Robert C. J., 1998, ARA&A, 36, 189
Kennicutt Robert C. J., Bresolin F., Garnett D. R., 2003, ApJ, 591, 801
Kewley L. J., Jansen R. A., Geller M. J., 2005, PASP, 117, 227
Kewley L. J., Groves B., Kauffmann G., Heckman T., 2006, MNRAS, 372, 961
Kewley L. J., Nicholls D. C., Sutherland R. S., 2019, ARA&A, 57, 511
Kobulnicky H. A., Kennicutt R. C. Jr, Pizagno J. L., 1999, ApJ, 514, 544
Köppen J., Hensler G., 2005, A&A, 434, 531
Koski A. T., 1978, ApJ, 223, 56
Koss M. J. et al., 2021, ApJS, 252, 29
Kraemer S. B., Wu C.-C., Crenshaw D. M., Harrington J. P., 1994, ApJ, 435, 171
Kroupa P., 2002, Science, 295, 82
Laursen P., Razoumov A. O., Sommer-Larsen J., 2009, ApJ, 696, 853
Leitherer C. et al., 1999, ApJS, 123, 3
Li S.-L., Grasha K., Krumholz M. R., Wisnioski E., Sutherland R. S., Kewley L. J., Chen Y.-M., Li Z., 2024, MNRAS, 529, 4993
Llerena M. et al., 2023, A&A, 676, A53
Luridiana V., Morisset C., Shaw R. A., 2015, A&A, 573, A42
MacAlpine G. M., 1988, PASP, 100, 65
Malkan M. A., Oke J. B., 1983, ApJ, 265, 92
Mannucci F. et al., 2021, MNRAS, 508, 1582
Matsuoka K., Nagao T., Maiolino R., Marconi A., Taniguchi Y., 2009, A&A, 503, 721
Matsuoka K., Nagao T., Marconi A., Maiolino R., Mannucci F., Cresci G., Terao K., Ikeda H., 2018, A&A, 616, L4
Mazzolari G. et al., 2024, preprint (arXiv:2408.15615)
McGaugh S. S., 1991, ApJ, 380, 140
de Mellos M. S. Z. et al., 2024, MNRAS, 535, 123
Mezcua M., Domínguez Sánchez H., 2024, MNRAS, 528, 5252
Mingozzi M. et al., 2022, ApJ, 939, 110
Mingozzi M. et al., 2024, ApJ, 962, 95
Molina M., Reines A. E., Latimer L. J., Baldassare V., Salehirad S., 2021, ApJ, 922, 155
Molina J., Ho L. C., Wang R., Shangguan J., Bauer F. E., Treister E., 2023, ApJ, 944, 30
Mollá M., Vílchez J. M., Gavilán M., Díaz A. I., 2006, MNRAS, 372, 1069
Monteiro A. F., Dors O. L., 2021, MNRAS, 508, 3023
Nagao T., Maiolino R., Marconi A., 2006, A&A, 447, 863
Nakajima K., Maiolino R., 2022, MNRAS, 513, 5134
Nakajima K. et al., 2018, A&A, 612, A94
Nicholls D. C., Sutherland R. S., Dopita M. A., Kewley L. J., Groves B. A., 2017, MNRAS, 466, 4403
Oliveira C. B., Krabbe A. C., Dors O. L., Zinchenko I. A., Hernandez-Jimenez J. A., Cardaci M. V., Hägele G. F., Ilha G. S., 2024, MNRAS, 531, 199
Onoue M. et al., 2020, ApJ, 898, 105

Osterbrock D. E., 1985, PASP, 97, 25
Osterbrock D. E., Martel A., 1993, ApJ, 414, 552
Pagel B. E. J., Edmunds M. G., Blackwell D. E., Chun M. S., Smith G., 1979, MNRAS, 189, 95
Peña-Guerrero M. A., Leitherer C., de Mink S., Wofford A., Kewley L., 2017, ApJ, 847, 107
Peimbert A., Peimbert M., 2010, ApJ, 724, 791
Peimbert M., Peimbert A., Delgado-Inglada G., 2017, PASP, 129, 082001
Peluso G., Radovich M., Moretti A., Mingozzi M., Vulcani B., Poggianti B. M., Marasco A., Gullieuszik M., 2023, ApJ, 958, 147
Pérez-Montero E., 2017, PASP, 129, 043001
Pérez-Montero E., Dors O. L., Vílchez J. M., García-Benito R., Cardaci M. V., Hägele G. F., 2019, MNRAS, 489, 2652
Pérez-Montero E., Amorín R., Pérez-Díaz B., Vílchez J. M., García-Benito R., 2023, MNRAS, 521, 1556
Phillips M. M., Charles P. A., Baldwin J. A., 1983, ApJ, 266, 485
Pilyugin L. S., Grebel E. K., Zinchenko I. A., Lara-López M. A., Nefedyev Y. A., Shulga V. M., 2020, A&A, 639, A96
Pilyugin L. S., Lara-López M. A., Vílchez J. M., Duarte Puertas S., Zinchenko I. A., Dors O. L., 2022, A&A, 668, A5
Revalski M., Crenshaw D. M., Kraemer S. B., Fischer T. C., Schmitt H. R., Machuca C., 2018, ApJ, 856, 46
Rigby J. R. et al., 2021, ApJ, 908, 154
Rizzuti F., Matteucci F., Molaro P., Cescutti G., Maiolino R., 2024, preprint (arXiv:2412.05363)
Roman-Duval J. et al., 2022, ApJ, 928, 90
Schmidt K. B. et al., 2021, A&A, 654, A80
Scholtz J. et al., 2023, preprint (arXiv:2311.18731)
Shields J. C., Ferland G. J., Peterson B. M., 1995, ApJ, 441, 507
Shirazi M., Brinchmann J., 2012, MNRAS, 421, 1043
Skillman E. D., Berg D. A., Pogge R. W., Moustakas J., Rogers N. S. J., Croxall K. V., 2020, ApJ, 894, 138
Snijders M. A. J., Netzer H., Boksenberg A., 1986, MNRAS, 222, 549
Storchi-Bergmann T., Schmitt H. R., Calzetti D., Kinney A. L., 1998, AJ, 115, 909
Storey P. J., Zeippen C. J., 2000, MNRAS, 312, 813
Sutherland R., Dopita M., Binette L., Groves B., 2018, Astrophysics Source Code Library, record ascl:1807.005
Tananbaum H. et al., 1979, ApJ, 234, L9
Tang J.-J. et al., 2019, MNRAS, 484, 2575
Thomas A. D., Dopita M. A., Kewley L. J., Groves B. A., Sutherland R. S., Hopkins A. M., Blanc G. A., 2018a, ApJ, 856, 89
Thomas A. D., Kewley L. J., Dopita M. A., Groves B. A., Hopkins A. M., Sutherland R. S., 2018b, ApJ, 861, L2
Toribio San Cipriano L., Domínguez-Guzmán G., Esteban C., García-Rojas J., Mesa-Delgado A., Bresolin F., Rodríguez M., Simón-Díaz S., 2017, MNRAS, 467, 3759
Véron-Cetty M. P., Véron P., 2006, A&A, 455, 773
Vidal-García A., Plat A., Curtis-Lake E., Feltre A., Hirschmann M., Chevallard J., Charlot S., 2024, MNRAS, 527, 7217
Walter D. K., Dufour R. J., Hester J. J., 1992, ApJ, 397, 196
Xu F., Bian F., Shen Y., Zuo W., Fan X., Zhu Z., 2018, MNRAS, 480, 345
Zhang X., 2024, ApJ, 960, 108
Zhu P., Kewley L. J., Sutherland R. S., 2023, ApJ, 954, 175
Zhu P., Kewley L. J., Sutherland R. S., 2024, ApJ, 977, 187
Zinchenko I. A., Dors O. L., Hägele G. F., Cardaci M. V., Krabbe A. C., 2019, MNRAS, 483, 1901

This paper has been typeset from a TEX/LATEX file prepared by the author.